The work reported in this document was performed at Lincoln Laboratory, a center for research operated by Massachusetts Institute of Technology. This work was supported by the Department of the Air Force under Contract F19628-80-C-0002, in part with specific funding from the Air Force Engineering and Services Center, Tyndall Air Force Base, Florida.

This report may be reproduced to satisfy needs of U.S. Government agencies.

The views and conclusions contained in this document are those of the contractor and should not be interpreted as necessarily representing the official policies, either expressed or implied, of the United States Government.

The Public Affairs Office has reviewed this report, and it is releasable to the National Technical Information Service, where it will be available to the general public, including foreign nationals.

This technical report has been reviewed and is approved for publication.

FOR THE COMMANDER

Thomas J. Alpert, Major, USAF
Chief, ESD Lincoln Laboratory Project Office

Non-Lincoln Recipients

PLEASE DO NOT RETURN

Permission is given to destroy this document when it is no longer needed.

AD A139448

20030109267

MASSACHUSETTS INSTITUTE OF TECHNOLOGY
LINCOLN LABORATORY

COHERENT LASER RADAR REMOTE SENSING

R.J. HULL
D.G. BIRON
S. MARCUS
J.H. SHAPIRO
Group 53

FINAL REPORT TO THE
AIR FORCE ENGINEERING AND SERVICES CENTER

1 OCTOBER 1982 — 30 SEPTEMBER 1983

ISSUED 19 JANUARY 1984

Approved for public release: distribution unlimited.

Ad-A 139448

LEXINGTON MASSACHUSETTS

ABSTRACT

This report summarizes the technical effort accomplished in FY83 on a program to make range-resolved measurements of chemical agents or pollutants distributed within the atmosphere. A description of the modified receiver electronics which permit rapid accumulation of a very large number of signal returns is described. The performance of a rapidly tunable CO_2 laser is discussed. Theoretical analyses of coherent laser radar systems including mixing efficiencies, speckle effects, and waveform performance are reported.

Accession For
NTIS GRA&I
DTIC TAB
Unannounced
Justification
Distribution/
Availability Codes
Avail and/or
Dist Special
A-1

TABLE OF CONTENTS

	ABSTRACT	iii
	LIST OF ILLUSTRATIONS	vi
I.	INTRODUCTION	1
II.	MODIFICATION OF RECEIVER ELECTRONICS	2
III.	FREQUENCY AGILE CO_2 LASER	4
IV.	THEORETICAL ANALYSES	8
V.	SUMMARY AND RECOMMENDATIONS	10
REFERENCES		11
APPENDIX A:	COHERENT LASER RADAR ANTENNA PATTERNS AND MIXING EFFICIENCIES	A-1
APPENDIX B:	RESOLUTION AND ACCURACY, AMBIGUITY AND ANOMALY FOR RANGE - SPREAD SPECKLE TARGETS	B-1
APPENDIX C:	PERFORMANCE ANALYSES FOR DOPPLER AND CHIRPED LASER RADARS	C-1

LIST OF ILLUSTRATIONS

1. Frequency-agile CO_2 laser 12

2. Laser output transient as transition was tuned from P(14) to P(20). 13

I. INTRODUCTION

This is the FY83 final report on a program entitled "Coherent Laser Radar Remote Sensing" supported by the Air Force Engineering and Services Center (AFESC) located at Tyndall Air Force Base. This effort is part of a program to assess the utility of using a coherent laser radar for the range-resolved detection and identification of chemical agents in the atmosphere. This work was begun in April 1982 and will continue through FY84. Previous research has been documented in the FY82 final report[1].

Specific tasks required under this program include 1) modifications to the existing transportable laser radar receiving electronics to permit recording of aerosol backscatter in several range bins on a single pulse, 2) field measurement of atmospheric aerosol backscatter cross-sections at single wavelength near 10.6μm with the modified electronics package, 3) modification of the laser transmitter to permit rapid switching between at least two separate wavelengths.

In section II of this report we describe the changes to the receiver electronics that are required and report on their status. Section III describes the progress made in constructing a laser rapidly tunable in wavelength by using an intracavity etalon. Several theoretical issues have been investigated and

are summarized in Section IV. These issues include optimization of heterodyne efficiency, decorrelation effects, and the use of other than a pulse waveform for achieving range resolution. Detailed technical descriptions of these issues have been included in three appendices.

II. MODIFICATIONS TO RECEIVER ELECTRONICS

The rationale for using a compact, coherent CO_2 laser radar to remotely sense concentrations of chemical agents was established in a previous report[1]. The basic radar performance theory for range-resolved aerosol return measurements was presented therein, along with experimental verifications[2] of the key premises of that theory: namely, signal strengths and statistics agreed well with theory. However, rapid data collection was hampered by the fact that the original electronics had been designed to operate on hard target returns. When operating against solid targets it is sufficient to record the strength and time of return of the single largest signal within the range-gate window. For the aerosol problem, the optical radar should be operated much like a conventional microwave radar, in which the signal propagates through space encountering many targets. Thus samples of the return signal should be recorded at many times from a single pulse.

The initial data were recorded in this mode through the use of a commercial digital oscilloscope with floppy-disk memory.

This set-up permitted recording signals at 75 different ranges between 0.2km and 1.5km on each pulse. Although the system runs at a pulse repetition frequency (PRF) of 20kHz, the collection time for 2,500 samples (pulses) of data was approximately 3 minutes in this mode owing to both a memory dump rate limitation and a memory size limitation in the oscilloscope. Receiver electronics have been built which will increase both the data acquisition rate and the amount of data stored. The system will run at an 8.66kHz pulse rate and collect and record signal strengths from 60 samples spaced at 100ft (30.5m) range intervals on each pulse. The acquisition window of 6000ft (1800m) may be placed anywhere within a setting of 0 and 20,000ft (6.1km). In practice returns from ranges less than 300m are ignored by the system.

This set of electronics is complete and is awaiting final "debugging" checks. When operational this system will permit acquiring data in times of approximately 1 second, which, when averaged, should permit making measurements with an accuracy of 1%. The experiments on the aerosol backscatter cross-section will then be repeated, and statistics gathered on the variability of this cross-section at a given time but at different look angles and also as a function of different weather conditions.

Single wavelength absorption measurements will then be made. A large absorption cell will be placed at a range of

approximately 3/4km from the radar. With the cell empty reference measurements of the backscatter will be made. By filling the cell with an absorbing gas (such as ethylene or sulfur hexafluoride), the sensitivity of the system may be established. This technique simulates dual wavelength Differential Absorption Lidar (DIAL) experiments. If the issues addressed in section III of this report can be solved this year a full dual wavelength, range resolved, remote sensing experiment will be attempted.

III. FREQUENCY AGILE CO_2 LASER

During FY83, we have implemented the intracavity tunable etalon technique for rapid tuning of the CO_2 laser between transitions. We employed a commercial etalon (Burleigh TL15IR), with a laboratory testbed laser. The etalon mirrors are coated for 80% reflectance at 10.6μm and spaced for a free spectral range of 50 cm^{-1}. This allows tuning over the entire P branch of the 10μm band.

The optical configuration is shown schematically in Figure 1. As the etalon is tuned monotonically, the laser output shifts from line to line, mostly between successive lines of the 10μm P branch. In the low-gain region of this spectrum, however the laser will occasionally emit at R-branch wavelengths or even in the 9μm band. This behavior is repeatable, as was demonstrated by applying a ramp voltage to the etalon. The non-P branch

oscillation could be suppressed, if desired, by appropriate coating of the laser output mirror, ensuring that all such competing lines are below oscillation threshold. Alternatively, the etalon spacing could be decreased by approximately a factor of 4 to bring these lines within the free spectral range. This, however, would also reduce the spectral resolution proportionally and hence the reliability with which a given line could be accessed.

If this type of laser is to be used in a differential absorption LIDAR (DIAL) system, it will have to be capable of switching rapidly between at least two prescribed transitions (on- and off- resonance). To demonstrate the capability, the laser was tuned to P(20), and a squarewave input pulse of variable amplitude was applied to the DC amplifier used to drive the etalon. By this means, we were able to switch back and forth between P(20) and any of 17 other lines at rapid rates, limited presumably only by the response of the piezoelectric transducer. Included in this group was the pair P(20), P(14) which can be used for DIAL measurements of C_2H_4 (ethylene) concentration. Another possible pair for C_2H_4 detection is P(12), P(14) for which rapid line shifting was also observed.

The primary advantage of this electronic tuning technique over conventional mechanical methods is its speed. To quantify this, a Ge:Au detector was used to monitor the transient output

as the laser was tuned from P(14) to P(20). As shown in Figure 2, the amplitude fluctuations decayed in several milliseconds. No attempt was made to damp these fluctuations.

One problem encountered with this approach is that the cavity length is, in general, not resonant for both transitions. Accordingly, the maximum power cannot be obtained from each of the sequentially tuned lines without also adjusting the total cavity length. We addressed this problem by applying the squarewave input to the D.C. amplifier controlling the main cavity length (as well as to the etalon driver) and adjusting the gain to maximize the laser power.

Another approach, which we have also implemented, is to change the gross cavity length such that the two relevant transitions may be simultaneously resonant. For the wavelengths involved, the required length change is invariably less than a centimeter, so that we were able to accomplish it by mounting a cavity mirror on a piezoeletric inchworm translator (1-inch total travel). This cavity retro-fit enabled us to tune sequentially between each member of any predetermined accessible line pair without also adjusting the cavity length with each line change.

Another concern when intracavity etalons are used is thermal stability. Indeed the laser required approximately a half-hour warm-up before approaching thermal equilibrium. After

this time, the etalon required periodic bias adjustment to maintain operation on a given line pair, but the required step voltage remained constant and was repeatable on a day-to-day basis. It is thus possible, once operation on a given line is achieved, to switch predictably to any other accessible transition. The required bias control would be achieved in an operational system by a servo control loop.

One disadvantage of the etalon technique of wavelength tuning is the large insertion loss of the etalon, which we measured to be 25% per pass. This resulted in a decrease in laser power from approximately 7 watts to 2 watts. That this power loss is so large is due to the fact that the testbed laser is relatively short (active length ≈ 50cm), and with the intracavity etalon, it operates very near threshold. We are currently fabricating a longer laser (active length ≈ 120cm) to be used as a testbed, for which this power reduction should be much less.

Another approach for reducing the etalon insertion loss is to reduce the mirror reflectance. The resulting decrease in power dissipation by the etalon should also reduce any thermal distortion. This change would also reduce the etalon's finesse and hence its resolving power, but a modest reduction in reflectance might improve the overall performance.

In conclusion, we have demonstrated the intracavity etalon technique for rapid wavelength tuning of a CO_2 laser. Areas for further study include multiple wavelength operation using multiple step driver waveforms and the effect of etalon mirror reflectance on laser performance. In addition, there remains the formidable task of frequency locking a local oscillator to the frequency-agile transmitter. In this regard, the pulsed-cw waveform for pulsed homodyne operation might be the most practical solution.

IV. THEORETICAL ANALYSES

The theoretical effort during FY83 was directed toward design-optimization issues for aerosol measurement laser radars. In particular, because of the weakness of aerosol returns relative to hard-target returns, against which compact CO_2 laser radars are customarily employed, maximization of heterodyne-mixing efficiency is critical for chemical agent detection. Moreover, because fielded systems may have to be multi-functional, mixing efficiency should be considered in conjunction with the spatial resolution of the radar, a characteristic critical to its hard-target imager function. Furthermore, Doppler-imaging radars, and range-imaging radars which use high time-bandwidth (TW) product waveforms, may also be part of the multi-functional panoply. Thus, the effects of

aerosol decorrelation on these long dwell time systems should be understood, so that the potential of such radars as chemical detectors can be assessed.

Results have been obtained and presented in all of the theoretical areas described above[3-5]. Their salient features are described below; the full papers cited appear as appendices to this report.

A. Antenna Patterns and Mixing Efficiencies[3]

The choice of transmitter and local-oscillator beam patterns affects both the spatial resolution capability (through the transmitting and receiving antenna patterns) and the carrier-to-noise ratio (through the heterodyne-mixing efficiency) of a coherent laser radar. We have made the first coordinated assessment of these effects. A monostatic shared-optics radar employing an unobscured circular-pupil objective (diameter D), a circular-pupil detector, and Gaussian transmitter and local-oscillator beams was considered. In far-field operation, parameter values were obtained yielding mixing efficiencies in excess of 80% and 25% for glint targets and speckle targets, respectively, and better than 0.8 λ/D angular resolution, where λ is the laser wavelength.

B. Resolution and Carrier-to-Noise Ratio[4,5]

The long pixel dwell times of Doppler laser radars and high TW product range-imaging laser radars make them susceptible to

performance degradation arising from target decorrelation. We have included target decorrelation, in addition to speckle effects, in analyses of velocity and range resolution and carrier-to-noise ratio (CNR) for such radars. Of particular interest for chemical agent detection is the fact that chirped-pulse range resolution degrades rapidly when the chirp duration T exceeds the aerosol correlation time (typically about 1μs), but the onset of significant CNR loss does not occur until this correlation time becomes smaller than the reciprocal chirp bandwidth 1/W. Because high TW operation with T > 1μs and W > 10MHz is assumed, chirped-pulse aerosol measurements are likely to suffer resolution loss but not CNR loss.

V. SUMMARY AND RECOMMENDATIONS

In FY82 range-resolved signal returns from naturally occurring atmospheric aerosols were observed from ranges up to 1.5km with the transportable coherent CO_2 laser radar system. The magnitude of the signals was approximately that expected theoretically. In FY83 modifications to the receiver electronics were designed and constructed that will permit accumulating range-resolved data at an 8.7kHz rate. In addition an intracavity etalon technique was used to demonstrate rapid tuning between pairs of lines across the 9μm to 11μm spectral band.

Theoretical analyses of waveforms other than pulse show decorrelation effects caused by the motion of the aerosols

during the measurement interval. These decorrelations produce a loss of range resolution but no loss in carrier-to-noise ratio. The optimum ratio of the relative sizes of the transmitter and receiver apertures was also obtained by analysis.

Work in FY84 is aimed at assessing the variability of the aerosol cross-sections and demonstrating a differential absorption measurement at a single wavelength of a known gas released into the atmosphere. If the problem of having the local oscillator wavelength track the transmitter wavelength can be solved in a timely fashion, then dual wavelength absorption measurements will be made.

REFERENCES

1. D. G. Biron, B. E. Edwards. S. Marcus, and R. J. Hull, "Coherent Laser Radar Remote Sensing," Final Report, Lincoln Laboratory, M.I.T. (30 September 1982, Issued 16 March 1983), DTIC AD-A127717/7.

2. D. G. Biron, "Aerosol Backscatter Measurements with a Coherent CO_2 Laser Radar," Technical Digest of Optical Techniques for Remote Probing of the Atmosphere (Incline Village, Nevada 1983).

3. J. H. Shapiro, V. E. Dardzinski, and E. W. Tung, "Coherent Laser Radar Antenna Patterns and Mixing Efficiency," Active Systems Speciality Group, IRIS (November 1983).

4. J. H. Shapiro, "Resolution and Accuracy, Ambiguity and Anomaly for Range-Spread Speckle Targets," Proc. SPIE 415, in press (1983).

5. J. H. Shapiro and P. L. Mesite, "Performance Analyses for Doppler and Chirped Laser Radars," Active Systems Specialty Group, IRIS (November 1983).

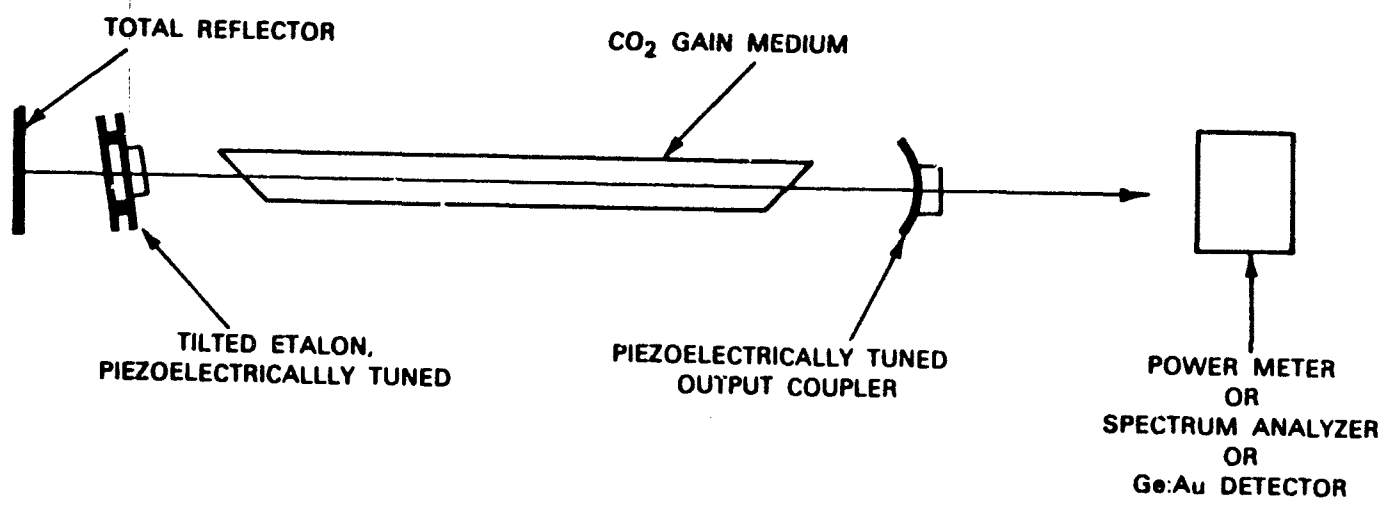

Fig. 1. Frequency-agile CO_2 laser.

135524-N

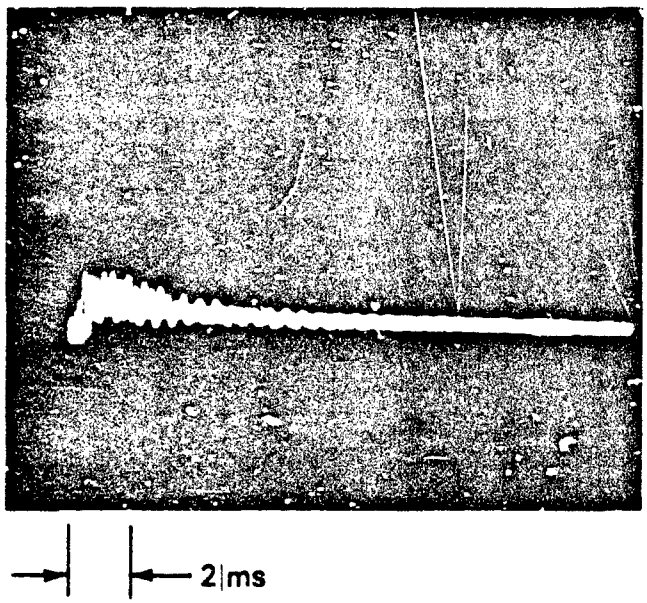

135525-R

Fig. 2. Laser output transient as transition was tuned from P(14) to P(20).

APPENDIX A

COHERENT LASER RADAR ANTENNA PATTERNS AND MIXING EFFICIENCIES*

6 September 1983

J. H. Shapiro
Massachusetts Institute of Technology
Department of Electrical Engineering and Computer Science
Cambridge, Massachusetts 02139

V. E. Dardzinski and E. W. Tung
Massachusetts Institute of Technology
Lincoln Laboratory
P.O. Box 73; Lexington, Massachusetts 02173

ABSTRACT

Transmitting and receiving antenna pattern expressions are developed for a monostatic coherent laser radar. These patterns are rigorously related to the standard glint-target and speckle-target monostatic radar equations to yield formulas for glint and speckle target mixing efficiencies. Numerical calculations for spatial resolution and mixing efficiency are presented for far-field operation using an untruncated-Gaussian transmitter beam and a Gaussian local-oscillator beam that has suffered both photodetector and objective-pupil truncation. Closed-form expressions for spatial resolution and mixing efficiency for an all Gaussian beam system are employed to assess the need for dynamic focusing in a large-aperture radar operating in the near field.

1.0 INTRODUCTION

Future requirements for high-resolution multifunction coherent CO_2 laser radars dictate a need for accurate system design methodologies. In particular, the choice of transmitter and local oscillator spatial beam patterns directly affects both the radar's spatial resolution capability (through the transmitting and receiving antenna patterns) and its carrier-to-noise ratio (through the heterodyne-mixing efficiency). Previous studies have not made a coordinated assessment of these effects. There is published work[1,2,3] on mixing

---

1. Degnan, J.J., and Klein, B.J., "Optical Antenna Gain 2: Receiving Antennas," Appl. Opt. 13, 2397-2401 (1974).

2. Fink, D., "Coherent Detection Signal-to-Noise," Appl. Opt. 14, 689-690 (1975).

3. Saga, N., Tanaka, K., and Fukumitsu, O., "Diffraction of a Gaussian Beam through a Finite Aperture Lens and the Resulting Heterodyne Efficiency," Appl. Opt. 20, 2827-2831 (1981).

*This work was sponsored by the Department of the Air Force.
"The US Government assumes no responsibility for the information presented".

efficiency as a function of local-oscillator beam pattern and photodetector diameter, but this work neglects the effects of target speckle and transmitter beam pattern on mixing efficiency, and those of local-oscillator beam pattern and photodetector diameter on the receiving antenna pattern. The work that has been published[4,5,6] on mixing efficiency including transmitter and speckle effects often assumes untruncated Gaussian beams, and generally does not examine the radar's spatial resolution. This paper addresses the joint dependence of spatial resolution and mixing efficiency on the transmitter and local oscillator beam patterns, eliminating some of the gaps left by earlier treatments.

Section 2.0 presents the system structure to be examined and the fundamental assumptions that are made. The analysis begins, in Section 3.0, with the development of antenna-pattern expressions. These are then rigorously related to the standard glint-target and speckle-target monostatic radar equations to yield formulas for glint and speckle target mixing efficiencies. Numerical calculations are presented in Section 4.0 for spatial resolution and mixing efficiency for far field operation using an untruncated-Gaussian transmitter beam and a Gaussian local-oscillator beam that has suffered both photodetector and objective-pupil truncation. Closed-form expressions for spatial resolution and mixing efficiency for an all Gaussian beam system are employed in Section 5.0 to assess the need for dynamic focusing in a large-aperture radar operating in the near field.

2.0 SYSTEM STRUCTURE

The system structure we shall consider, shown schematically in Fig. 1, is a monostatic shared-optics coherent laser radar using a single photodetector and

---

4. An all Gaussian beam signal-to-noise ratio calculation for a monostatic radar viewing a speckle target appears in Sonnenschein, C.M., and Horrigan, F.A., "Signal-to-Noise Relationships for Coaxial Systems that Heterodyne Backscatter from the Atmosphere," Appl. Opt. 10, 1600-1604 (1971). This work neglects atmospheric turbulence, and does not examine spatial resolution.

5. All Gaussian beam speckle-target mixing efficiency including the effects of atmospheric turbulence was treated by Yura, H.T., "Signal-to-Noise Ratio of Heterodyne Lidar Systems in the Presence of Atmospheric Turbulence," Optica Acta 26, 627-644 (1979), and Clifford, S.F., and Wandzura, S., "Monostatic Heterodyne Lidar Performance: The Effect of the Turbulent Atmosphere," Appl. Opt. 20, 514-516 (1981). Neither work studied spatial resolution.

6. Mixing efficiency for truncated Gaussian beam radars has been analyzed in Rye, B.J., "Antenna Patterns for Incoherent Backscatter Heterodyne Lidar," Appl. Opt. 18, 1390-1398 (1979) and calculations have been reported by Leader, J.C., "Detection Efficiency for Large-Aperture Coherent Laser Radars," Proc. SPIE 300, 74-85 (1981), and Wang, J.Y., "Heterodyne Laser Radar SNR from a Diffuse Target Containing Multiple Glints," Appl. Opt. 21, 464-475 (1982). The latter two studies include atmospheric turbulence; none of these papers considers spatial resolution per se.

unobscured circular pupil refractive optics[7]. The transmitter and local-oscillator beams entering the transmit/receive (TR) switch are both TEM_{00} untruncated Gaussians. These beams are such that the normalized transmitter spatial beam pattern as it leaves the objective lens is

$$\xi_T(\bar{\rho}) = (2/\pi a_T^2)^{1/2} \exp[-|\bar{\rho}|^2 (a_T^{-2} + jk/2R)], \tag{1}$$

and the normalized local-oscillator spatial beam pattern as it impinges on the photodetector is

$$\xi_L(\bar{\rho}) = (2/\pi a_{DL}^2)^{1/2} \exp[-|\bar{\rho}|^2 (a_{DL}^{-2} - jk/2\ell)], \tag{2}$$

for $\bar{\rho} = (x,y)$ the transverse coordinate vector, and $k = 2\pi/\lambda$ the wavenumber at the radar wavelength λ. Here, a_T and a_{DL} are e^{-2} intensity radii of the transmitter and local oscillator beams at the objective lens and the photodetector, respectively. The transmitter beam (1) has a phase radius of curvature corresponding to a geometric-optics focus located R (R>0) meters in front of the objective, implying a Gaussian beam waist located $R/(1+\Omega^{-2})$ meters in front of the objective where $\Omega = ka_T^2/2R$. The local-oscillator beam (2) has a phase radius of curvature such that were $\xi_L^*(\bar{\rho})$ backpropagated through the optical system the beam exiting the objective lens would have e^{-2} intensity radius

$$a_L = \lambda\ell/\pi a_{DL}, \tag{3}$$

and the same phase radius of curvature

$$R = (f^{-1} - \ell^{-1})^{-1}, \tag{4}$$

as the transmitter beam, where f is the focal length of the objective lens.

The preceding Gaussian-beam descriptions ignore the truncation effects imposed by the finite photodetector diameter d (on the local oscillator), and by the finite pupil diameter D (on the transmitter and the backpropagated local oscillator). Because transmitter truncation entails a loss of transmitter power, which is generally at a premium, we shall assume $D \geq 4a_T$, a condition that ensures transmitter truncation is negligible in terms of both power and target-plane beam pattern. There is no similarly high premium on the local-oscillator power, so in general that beam may be subject to both of the truncation effects noted above. In what follows, (3) will be used to define a_L, and (4) to relate

---

7. The formulas we derive apply as well to unobscured reflective optics such as those employed in the Lincoln Laboratory test bed radar, see Harney, R.C., and Hull, R.J., "Compact Infrared Radar Technology," Proc. SPIE 227, 162-170 (1980).

R, ℓ, and the objective focal length f, even though the backpropagated local-oscillator field leaving the objective pupil need not be Gaussian. Thus, the parameters a_L and R cease having the physical interpretations given with (3), (4) unless $d \geq 4a_{DL}$ and $D \geq 4a_L$ both prevail.

In any case, the target of interest will be assumed to be a stationary object that is unresolved in range (planar) and at a distance L m in front of the radar. The target will either be a spatially unresolved on-axis glint object of radar cross-section σ m^2, or a spatially resolved speckle object of uniform diffuse reflectivity ρ sr^{-1}. The atmosphere will be assumed to be non-turbulent with an extinction coefficient α m^{-1}. All losses in the radar optics (not associated with local-oscillator truncation) will be neglected. The photodetector will be taken to have quantum efficiency η.

3.0 BASIC RESULTS

The normalized intermediate-frequency (IF) photocurrent for the radar shown in Fig. 1 has complex envelope[8]

$$\underline{r}(t) = \underline{y} + \underline{n}(t) \tag{5}$$

consisting of a target return y plus local-oscillator shot nosie $\underline{n}(t)$. Via the antenna theorem for heterodyne detection[9], the former is conveniently expressed as a target-plane integral[8,10,11]

$$\underline{y} = P_T^{1/2} \int d\bar{\rho}\ \underline{T}(\bar{\rho})\ \underline{\xi}_T'(\bar{\rho})\ \underline{\xi}_R'(\bar{\rho}) , \tag{6}$$

in terms of the transmitter power P_T, the transmitter pattern $\underline{\xi}_T'(\bar{\rho})$ resulting from propagating $\underline{\xi}_T(\bar{\rho})$ over the L-meter atmospheric path, the receiver pattern $\underline{\xi}_R'(\bar{\rho})$ resulting from truncating and renormalizing $\underline{\xi}_L^*(\bar{\rho})$ on the detector pupil then backpropagating through the optical system and over the L-meter atmospheric path, and the target's complex-field reflection coefficient

---

8. The system model we shall employ parallels that developed in Shapiro, J.H., Capron, B.A., and Harney, R.C., "Imaging and Target Detection with a Heterodyne-Reception Optical Radar," Appl. Opt. 20, 3292-3313 (1981).

9. Siegman, A.E., "The Antenna Properties of Optical Heterodyne Receivers," Proc. IEEE 54, 1350-1356 (1966).

10. Rye, B.J., "Refractive-Index Turbulence Contribution to Incoherent Backscatter Heterodyne Lidar Returns," J. Opt. Soc. Am. 71, 687-691 (1981).

11. Papurt, D.M., Shapiro, J.H., and Harney, R.C., "Atmospheric Propagation Effects on Coherent Laser Radars," Proc. SPIE 300, 86-99 (1981).

$\underline{T}(\bar{\rho})$. Via well known results for heterodyne detection[12], the noise $\underline{n}(t)$ is a zero-mean circulo-complex white Gaussian process of spectral height $h\nu_o/\eta$, in terms of the photon energy at the radar's optical frequency $\nu_o = c/\lambda$.

3.1 GLINT TARGET RESULTS

The glint target under consideration is spatially unresolved, thus the only performance measure to be evaluated for this case is the carrier-to-noise ratio (CNR), namely the ratio of target-return power to average noise power in a B Hz IF bandwidth. By means of previous work[13], we know that the CNR obeys the monostatic radar equation

$$\mathrm{CNR} = \frac{\eta P_T}{h\nu_o B} \frac{G_T}{4\pi L^2} \frac{\sigma A_R^g}{4\pi L^2} e^{-2\alpha L} , \tag{7}$$

where

$$G_T = 4\pi L^2 e^{\alpha L} \left|\xi_T'(\bar{0})\right|^2 , \tag{8}$$

is the transmitter antenna gain, and

$$A_R^g = (\lambda L)^2 e^{\alpha L} \left|\xi_R'(\bar{0})\right|^2 \tag{9}$$

is the effective heterodyne-detection glint-target mixing area. Equation (7) is the standard glint-target result if A_R^g is set equal to the objective pupil area $\pi D^2/4$. It is a simple Fourier optics calculation to show that $A_R^g \leq \pi D^2/4$, so that we may usefully define

$$\varepsilon_{het}^g = 4A_R^g/\pi D^2, \tag{10}$$

as the glint-target monostatic radar heterodyne mixing efficiency.

3.2 SPECKLE TARGET RESULTS

For a resolved speckle target of non-uniform reflectivity the average target return power obeys[8,11]

$$\langle|\underline{y}|^2\rangle = P_T\lambda^2 \int d\bar{\rho}\, T(\bar{\rho}) \left|\xi_T'(\bar{\rho})\right|^2 \left|\xi_R'(\bar{\rho})\right|^2 , \tag{11}$$

where $T(\bar{\rho})$ is the average intensity reflection profile of the target. Evidently, the spatial resolution of the radar (at range L) is determined by the transmitter

---

12. Gagliardi, R. M., and Karp, S., Optical Communications (Wiley, New York, 1976) Chap. 6.

13. Shapiro, J.H., "Target-Reflectivity Theory for Coherent Laser Radars," Appl. Opt. 21, 3398-3407 (1982).

antenna pattern

$$\zeta_T(\bar{\rho}) = \left|\xi_T'(\bar{\rho})/\xi_T'(\bar{0})\right|^2 , \tag{12}$$

and the receiver antenna pattern

$$\zeta_R(\bar{\rho}) = \left|\xi_R'(\bar{\rho})/\xi_R'(\bar{0})\right|^2 , \tag{13}$$

where we have assumed that the denominator terms in (12) and (13) are non-zero. In particular, the nominal spatial resolution of the radar will be taken to equal the $|\bar{\rho}|$ value necessary to drive the composite antenna pattern $\zeta_T(\bar{\rho})\zeta_R(\bar{\rho})$ from its on-axis value of unity to a value of e^{-2}. (Note that our system structure forces the antenna patterns to depend only on $|\bar{\rho}|$.) In far-field operation the spatial resolution will be proportional to L, i.e., the radar has a fixed far-field angular resolution.

Suppose that the target profile $T(\bar{\rho})$ corresponds to a uniform diffuse reflectivity ρ, viz.[13] $T = \rho/\pi$, over the spatial resolution cell probed by the radar. It then follows that the speckle-target CNR obeys

$$\mathrm{CNR} = \frac{\eta P_T}{h\nu_o B} \frac{\rho A_R^{\,s}}{\pi L^2} e^{-2\alpha L} , \tag{14}$$

where

$$A_R^{\,s} = (\lambda L)^2 e^{2\alpha L} \int d\bar{\rho} \left|\xi_T'(\bar{\rho})\right|^2 \left|\xi_R'(\bar{\rho})\right|^2 , \tag{15}$$

is the effective heterodyne-detection speckle-target mixing area. Once again, this is the standard CNR result if $A_R^s = \pi D^2/4$, and Fourier optics can be used to prove $A_R^s \leq \pi D^2/4$. Thus, we define

$$\epsilon_{het}^{\,s} = 4A_R^{\,s}/\pi D^2 , \tag{16}$$

as the speckle-target monostatic radar heterodyne mixing efficiency.

4.0 FAR-FIELD CALCULATIONS

In this section we shall present calculations for the case of far-field operation ($kD^2/4L \ll 1$) with the radar focused at infinity ($R = \infty$, $\ell = f$). Here our main effort will be to study the effects of local oscillator truncation on spatial resolution and mixing efficiency.

4.1 GLINT TARGET CALCULATIONS

Under the propagation conditions cited above, the basic glint-target results take the form given in Section 3.1 with

$$G_T = 2k^2 a_T^{\,2} , \tag{17}$$

and (after some manipulation)

$$\epsilon_{het}{}^{g} = \frac{(\pi\mu_L)^2 \left[\int_0^{\gamma} dy \exp[-(\pi\mu_L y/4)^2] J_1(\pi y)\right]^2}{2[1 - \exp[-(\pi\mu_L\gamma)^2/8]]} , \tag{18}$$

where J_1 is a Bessel function,

$$\mu_L = 4a_L/D , \tag{19}$$

and

$$\gamma = Dd/2\lambda f . \tag{20}$$

The dimensionless parameters μ_L and γ are key physical entities: μ_L measures the backpropagated local oscillator size (in the absence of photodetector truncation, $4a_{DL}/d \leq 1$) relative to the objective diameter; γ measures the detector size relative to the focal-plane diffraction width of the objective. Both parameters can be expected to be of order of magnitude unity in realistic system designs.

Two important special cases of Eq. (18) are easily developed. When $4a_{DL}/d \gg 1$ (equivalent to $8/\pi\mu_L\gamma \gg 1$) the local-oscillator beam (2) has an essentially uniform intensity over the diameter d detector; it can then be shown that

$$\epsilon_{het}{}^{g} = [2(1 - J_0(\pi\gamma))/\pi\gamma]^2 . \tag{21}$$

On the other hand, when $4a_{DL}/d \leq 1$ and $4a_L/D \leq 1$ (equivalent to $8/\pi\mu_L\gamma \leq 1$ and $\mu_L \leq 1$) there is no truncation of the local oscillator on the detector nor is there any (after backpropagation) at the objective lens; for this case

$$\epsilon_{het}{}^{g} = \mu_L{}^2/2 . \tag{22}$$

In Fig. 2, we have plotted $\epsilon_{het}{}^{g}$ (from Eq. (20)) vs. γ for a variety of μ_L values. For a fixed transmitter beam and objective lens, this amounts to plotting glint-target mixing efficiency vs. normalized photodetector diameter for various normalized local-oscillator intensity radii. We see from Fig. 2 that for each μ_L value there is an optimum γ value at which $\epsilon_{het}{}^{g}$ is maximized. We also see $\epsilon_{het}{}^{g} \geq 0.8$ is attainable within the parameter set we have plotted.

Note that as the photodetector diameter tends toward zero ($\gamma \to 0$) all the $\epsilon_{het}{}^{g}$ curves coincide with the uniform local-oscillator ($\mu_L = 0$) case, going to zero efficiency in the zero-diameter limit. When the photodetector diameter becomes very large ($\gamma \to \infty$) all the $\epsilon_{het}{}^{g}$ curves approach asymptotes set by μ_L, viz. (18) reduces to

$$\epsilon_{het}{}^{g} = \mu_L{}^2 \{1 - \exp(-4/\mu_L{}^2)\}^2/2 \ . \tag{23}$$

From (23), the large-γ $\epsilon_{het}{}^{g}$ asymptotes can be shown to approach zero when $\mu_L \to 0$ and $\mu_L \to \infty$; their maximum value occurs near $\mu_L = 1.7$. Finally, because of Bessel function oscillations, the $\gamma \to \infty$ asymptotes are not achieved monotonically.

To those accustomed to one-way propagation (i.e., laser communication rather than laser radar) heterodyne mixing efficiency calculations[1-3], Fig. 2 may at first present some puzzling features. It is well known that unity heterodyne mixing efficiency results in the communication problem if the detector diameter d greatly exceeds the focal-plane width of the signal intensity pattern and the local oscillator field pattern exactly matches the signal field pattern on the detector. It might seem, therefore, that in the radar calculation $\epsilon_{het}{}^{g}$ will achieve its maximum value (if not unity) when the detector is large and the local oscillator beam (2) is matched to the transmitter beam (1), viz. $8/\pi\mu_L\gamma \leq 1$ with $\mu_L = \mu_T \equiv 4a_T/D$. Because of our no-truncation assumption at the transmitter we have $\mu_T \leq 1$, and thus (22) applies, giving $\epsilon_{het}{}^{g} \leq 0.5$ for this "matched" case. Even the maximum $\epsilon_{het}{}^{g}$ value over γ and $\mu_L \leq 1$ is still less than the maximum $\epsilon_{het}{}^{g}$ value over γ and μ_L, as the latter occurs at $\mu_L > 1$.

Physically there is no conflict between Fig. 2 and the laser communication dictum of matching the local oscillator to the signal over the detector. Equation (1) is the signal field leaving the transmitter and Eq. (2) is the local oscillator field impinging on the detector. For an unresolved glint target, the target-return field impinging on the detector will be a Bessel function circular-pupil diffraction pattern. Indeed the integral on the right in (18) is the overlap integral of this Bessel function pattern and the Gaussian local oscillator pattern. That $\epsilon_{het}{}^{g}$ has a maximum value at fixed a_{DL} as d is

varied is therefore exactly like the laser communication mixing efficiency calculation for a plane signal wave incident on an objective lens being mixed on a focal plane detector with a Gaussian local-oscillator field[3,14].

4.2 SPECKLE TARGET CALCULATIONS

For far-field propagation with the radar focused at infinity, the basic speckle-target results take the form given in Section 3.2 with

$$\zeta_T(\bar{\rho}) = \exp[-(\pi\mu_T x)^2/8] \quad , \tag{24}$$

$$\zeta_R(\bar{\rho}) = \left[\frac{\int_0^\gamma dy\ y \exp[-(\pi\mu_L y/4)^2]\ F(x,y)}{\int_0^\gamma dy \exp[-(\pi\mu_L y/4)^2]\ J_1(\pi y)} \right]^2 , \tag{25}$$

and

$$\epsilon_{het}^{s} = \epsilon_{het}^{g}\ (\pi\mu_T/2)^2 \int_0^\infty dx\ x\ g_T(x)\ g_R(x) \ , \tag{26}$$

where

$$x = D\ |\bar{\rho}|/\lambda L \tag{27}$$

measures the transverse distance in the target plane relative to the nominal far-field diffraction scale of the objective lens,

$$\mu_T = 4a_T/D \leq 1 \tag{28}$$

measures the transmitter beam relative to the objective diameter ($\mu_T \leq 1$ is our no transmitter-beam truncation assumption),

$$F(x,y) = \int_0^{2\pi} d\theta\ (2\pi z)^{-1}\ J_1(\pi z), \tag{29}$$

for

$$z = (x^2 + y^2 - 2xy\cos\theta)^{1/2} \ , \tag{30}$$

and

$$g_i(D|\bar{\rho}|/\lambda L) = \zeta_i(\bar{\rho}), \text{ for } i = T,\ R, \tag{31}$$

are the transmitter and receiver angular patterns normalized to the λ/D diffraction scale.

As was the case in Section 4.1, it is worth considering the special cases of the uniform local oscillator ($8/\pi\mu_L\gamma \gg 1$), and the untruncated local

---

14. Cohen, S.C., "Heterodyne Detection: Phase Front Alignment, Beam Spot Size, and Detector Uniformity," Appl. Opt. 14, 1953-1959 (1975).

oscillator ($8/\pi\mu_L\gamma \leq 1$ and $\mu_L \leq 1$). In the former instance we find

$$\zeta_R(\bar{\rho}) = \pi^2[1 - J_0(\pi\gamma)]^{-2}\, G(y), \tag{32}$$

$$\epsilon_{het}{}^s = (2\pi\mu_T)^2 \int_0^\infty dy\; y \exp[-(\pi\mu_T\gamma y)^2/2]\; G(y), \tag{33}$$

where

$$y = |\bar{\rho}|f/dL \tag{34}$$

measures transverse distance in the target plane relative to the geometric projection of the detector diameter onto the target plane, and

$$G(y) = [\int_0^\gamma dx\; J_1(\pi x)\; J_0(2\pi xy)]^2 \quad . \tag{35}$$

In the latter case we obtain

$$\zeta_R(\bar{\rho}) = \exp[-(\pi\mu_L x)^2/8] \ , \tag{36}$$

and

$$\epsilon_{het}{}^s = \mu_T{}^2\mu_L{}^2/2(\mu_T{}^2 + \mu_L{}^2) \ , \tag{37}$$

where x is defined in (27).

Let us first use the foregoing results to examine the radar's spatial resolution. The composite beam pattern $\zeta_T(\bar{\rho})\zeta_R(\bar{\rho})$ is the product of a simple Gaussian ζ_T with e^{-2} radius $x = 4/\pi\mu_T$ (equivalent to $|\bar{\rho}| = \lambda L/\pi a_T$) and a complicated ζ_R from Eq. (25). In Figs. 3 and 4 we have plotted the angular pattern $g_R(x)$ vs. x for $\mu_L = 0.5$ and 1.7, respectively, and a variety of γ values. From these figures the following characteristics may be discerned. For small μ_L and large γ the beam pattern broadens, approaching the Gaussian (36) with e^{-2} radius $x = 4/\pi\mu_L$ (equivalent to $|\bar{\rho}| = \lambda L/\pi a_L = La_{DL}/f$), as expected. For μ_L large or γ small, the beam pattern approaches Airy disk behavior, with a deep null near $x = 1.22$ (equivalent to $|\bar{\rho}| = 1.22\ \lambda L/D$). Physically, the second case corresponds to a uniform local oscillator over a detector that is unresolved by the objective lens, from which we derive, via (32) with $\gamma \ll 1$,

$$\zeta_R(\bar{\rho}) \rightarrow [2J_1(\pi x)/\pi x]^2 \ . \tag{38}$$

The implications of the above results are really not surprising. When the local oscillator is essentially untruncated $\zeta_R(\bar{\rho})$ is broader than the $\lambda L/D$ objective-lens diffraction width. When the uniform local oscillator assumption

is valid, $\zeta_R(\bar{\rho})$ is roughly $\lambda L/D$ in radius. For the untruncated case we obtain the closed-form expression

$$r_{res} = \lambda L/\pi(a_T^2 + a_L^2)^{1/2} \quad , \tag{39}$$

for the e^{-2} radius of $\zeta_T(\bar{\rho})\zeta_R(\bar{\rho})$. Generally speaking, increasing a_L so that local oscillator truncation is incurred improves spatial resolution somewhat, but the resolution is never better than about 0.7 $\lambda L/D$ when the maximum $a_T = D/4$ is employed. (Note that the reason resolution exceeds the 1.22 $\lambda L/D$ Rayleigh criterion is because we are concerned with the e^{-2} radius rather than the radius to the first zero of the composite antenna pattern).

Let us turn now to the behavior of $\epsilon_{het}{}^s$, which we have plotted vs. γ in Figs. 5 and 6 for $\mu_T = 0.7$ and 1.0, respectively, and various μ_L values. These figures share many of the features found in the $\epsilon_{het}{}^g$ curves from Fig. 2. In particular: $\epsilon_{het}{}^s$ has a maximum value for each μ_T, μ_L pair as γ is varied; as the detector diameter tends toward zero ($\gamma \to 0$), all the $\epsilon_{het}{}^s$ curves coincide (corresponding to the uniform local oscillator limit) and approach zero efficiency; and as the detector diameter becomes very large ($\gamma \to \infty$) all the $\epsilon_{het}{}^g$ curves approach asymptotes set by their μ_L, μ_T values, which for fixed μ_T go to zero if $\mu_L \to 0$ or $\mu_L \to \infty$. The speckle target mixing efficiencies are appreciably lower than the glint-target efficiencies, with $\epsilon_{het}{}^s = 0.28$ being the maximum attainable value within the parameter set we have plotted. Part of this reduction is forced upon us by the no-truncation assumption $\mu_T \leq 1$; it is a simple Fourier optics calculation to show from (8), (15),(16) that

$$\epsilon_{het}{}^s \leq 4(\lambda L)^2 e^{\alpha L} \left|\underline{\xi}_T'(\bar{0})\right|^2/\pi D^2 = \mu_T^2/2 \leq 0.5 \quad . \tag{40}$$

Thus, $\epsilon_{het}{}^s = 0.28$ actually corresponds to a 56% efficiency vis a vis the transmitter limit given in (40). Note that, as was found for $\epsilon_{het}{}^g$ in Fig. 2, this maximum is not reached with "matched" operation (i.e., $8/\pi\mu_L\gamma \leq 1$ with $\mu_L = \mu_T \leq 1$), the reason being that the preceding conditions do not best match the local oscillator to the target-return signal on the photodetector. We ascribe the observed $\epsilon_{het}{}^s < \epsilon_{het}{}^g$ behavior to the partial coherence over the objective lens of the target-return field from the resolved speckle target, as opposed to the complete coherence of the glint-target return over this lens.

5.0 NEAR-FIELD CALCULATIONS

It was pointed out quite some time ago[15] that a monostatic coherent laser radar that is focused at infinity will suffer a very significant loss in heterodyne efficiency when viewing targets located in the radar's near field. Gaussian-beam radar calculations show[15] that best near-field mixing efficiency results when the transmitter beam and the backpropagated local-oscillator beam have their geometric optics foci at the target plane. Because future high-resolution coherent laser radars may have near fields extending 2 to 4 km, the preceding focus effects must be considered. Owing to the complexity of near-field patterns for backpropagated local oscillator beams with truncation, we shall limit our treatment of the near-field problem to the untruncated ($4a_{DL}/d \leq 1$, $4a_L/D \leq 1$) Gaussian beam regime.

5.1 NEAR-FIELD RESOLUTION

The near-field propagation untruncated Gaussian beam patterns are

$$\zeta_T(\bar{\rho}) = \exp[-(\pi u_T x)^2/8(1 + \Omega_T^2)] \quad , \tag{41}$$

and

$$\zeta_R(\bar{\rho}) = \exp[-(\pi u_L x)^2/8(1 + \Omega_R^2)] \quad , \tag{42}$$

where u_T, u_L, and x are as in Section 4.0, and

$$\Omega_T = ka_T^2 \left|R^{-1} - L^{-1}\right|/2 \quad , \tag{43}$$

$$\Omega_R = ka_L^2 \left|R^{-1} - L^{-1}\right|/2 \quad , \tag{44}$$

are dimensionless near-field focusing factors. When the transmitter and backpropagated local oscillator have their geometric foci at the target range (R = L), Eqs. (41) and (42) reduce to the far-field formulas (24) and (36), respectively, as expected. The near-field spatial resolution, given by the e^{-2} radius of $\zeta_T(\bar{\rho})\zeta_R(\bar{\rho})$ is easily found to be

$$r_{res} = \lambda L/\pi[a_T^2/(1 + \Omega_T^2) + a_L^2/(1 + \Omega_R^2)]^{1/2} \quad , \tag{45}$$

which simplifies to become (39) when R = L.

---

15. Sonnenschein, C.M., and Horrigan, F.A., "Signal-to-Noise Relationships for Coaxial Systems that Heterodyne Backscatter from the Atmosphere," Appl. Opt. 10, 1600-1604 (1971).

Because Ω_T and Ω_R are positive for $R \neq L$, we see that resolution degrades in the near field when the geometric-optics beam foci do not coincide with the target range. We can use (45) to quantitatively assess whether the foregoing degradation is sufficient that high-resolution near-field radars must use dynamic focusing to match R to L for each target in the scanned field of view. In Fig. 7, for example, we plot r_{res} vs. range L for $\lambda = 10.6$ μm with $a_T = a_L = 7.23$ cm and various choices of R. These a_T, a_L values give 33 μrad far-field angular resolution when collimated beams ($R = \infty$) are employed, in which case the near field to far field transition begins at about L = 1.5 km. Three R choices are shown in Fig. 7: R = 2 km (fixed geometric-optics focus at 2 km), $R = \infty$ (collimated-beam operation), and R = L (dynamic focusing). Over a nominal 1 km to 5 km range interval, Fig. 7 indicates that fairly comparable resolution is achieved by the three R choices plotted, implying that dynamic focusing is not critical for good resolution in this case.

5.2 NEAR-FIELD MIXING EFFICIENCIES

The preceding near-field propagation untruncated Gaussian beam patterns give rise to mixing efficiencies

$$\epsilon_{het}{}^{g} = \mu_L{}^2/2(1 + \Omega_R{}^2) \quad , \tag{46}$$

for a glint target, and

$$\epsilon_{het}{}^{s} = 1/2[(1 + \Omega_T{}^2)/\mu_T{}^2 + (1 + \Omega_R{}^2)/\mu_L{}^2] \ , \tag{47}$$

for a speckle target. Recall that we are referencing our heterodyne-mixing areas to the objective lens area $\pi D^2/4$ to obtain these efficiencies (see Eqs. (9), (10), (15), (16)), so that the no-truncation assumptions $\mu_T \leq 1$ and $\mu_L \leq 1$ imply $\epsilon_{het}{}^g \leq 0.5$ and $\epsilon_{het}{}^s \leq 0.25$. These maximum Gaussian-beam efficiencies are achieved when $\mu_T = \mu_L = 1$, and R = L, and the glint-target result is significantly lower than the best far-field truncated local oscillator $\epsilon_{het}{}^g$ from Fig. 2.

As was found for near-field resolution, Ω_T and Ω_R being positive for $R \neq L$ will degrade mixing efficiency. In Fig. 8 we plot $\epsilon_{het}{}^g$ and $\epsilon_{het}{}^s$ vs. range L for the radar considered in Section 5.1, namely $\lambda = 10.6$ μm, $a_T = a_L = 7.23$ cm, with R = 2 km, ∞, or L, and $\mu_T = \mu_L = 1$. (Because $a_T = a_L$, (46) and (47) yield $\epsilon_{het}{}^s = \epsilon_{het}{}^g/2$.) Whereas the spatial resolution was not severely affected by the choice of geometric-optics focal distance R, Fig. 8 shows that mixing efficiency is a strong function of R. Figure 8 shows that

choosing R = 2 km achieves better than 80% of the optimum (R = L) mixing efficiency over the range interval from 1.2 km to 5.5 km, and outperforms collimated-beam (R = ∞) operation over the range interval from 0.5 km to 4 km. Thus, dynamic focusing does not appear to be necessary here.

6.0 CONCLUSIONS

We have tried to provide a rigorous construct for assessing the spatial resolution and heterodyne mixing efficiency of a monostatic coherent laser radar. The basic results in Section 3.0 have rather general applicability, e.g., they could be used to study performance for Cassegrain telescopes by changing ξ_T' and ξ_R' appropriately[16]. The results of Section 4.0 indicate that "matched" operation of an untruncated Gaussian transmitter beam and an untruncated Gaussian local oscillator beam does not optimize system performance[17]. The results of Section 5.0 imply that fixed focus near-field operation may be the logical approach to high resolution radars, as dynamic focusing may not offer performance benefits sufficient to warrant the concomitant system complexity. Finally, we should point out that atmospheric turbulence effects should be included for a more complete treatment of spatial resolution and mixing efficiency of large-aperture radars.

---

16. Greene, B.A., Masters, D., Rye, B.J., and Thomas, E.L., "Antenna Considerations in Atmospheric Backscatter Coherent Lidar," Technical Digest of Topical Meeting on Coherent Laser Radar for Atmospheric Sensing (Opt. Soc. Am., Aspen, 1980) paper TuB3.

17. Wang, J.Y., "Heterodyne Laser Radar Performance," Proc. SPIE 300, 110-117 (1981).

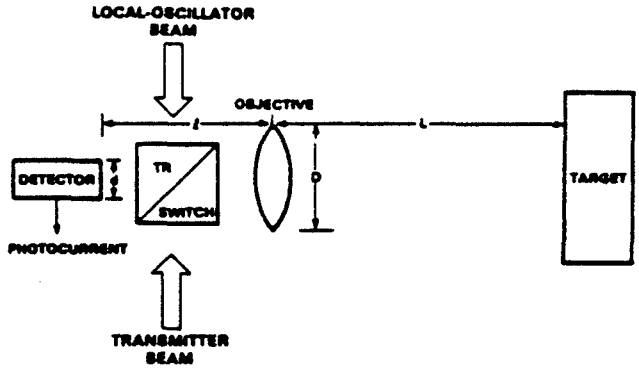

FIGURE 1. MONOSTATIC COHERENT LASER RADAR SYSTEM STRUCTURE.

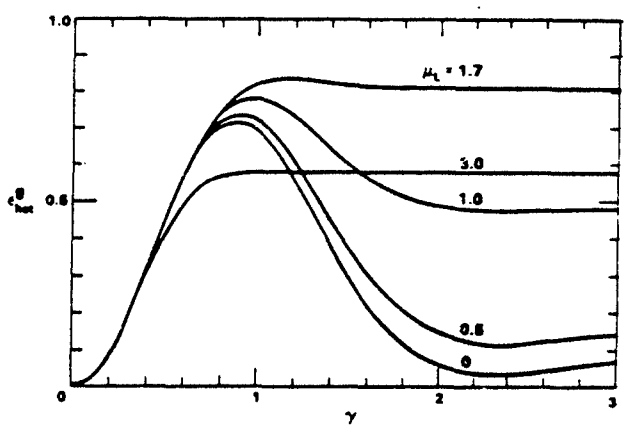

FIGURE 2. FAR-FIELD GLINT-TARGET MIXING EFFICIENCY ϵ_{het}^{g} vs. NORMALIZED DETECTOR DIAMETER γ FOR VARIOUS VALUES OF NORMALIZED LOCAL-OSCILLATOR INTENSITY RADIUS μ_L.

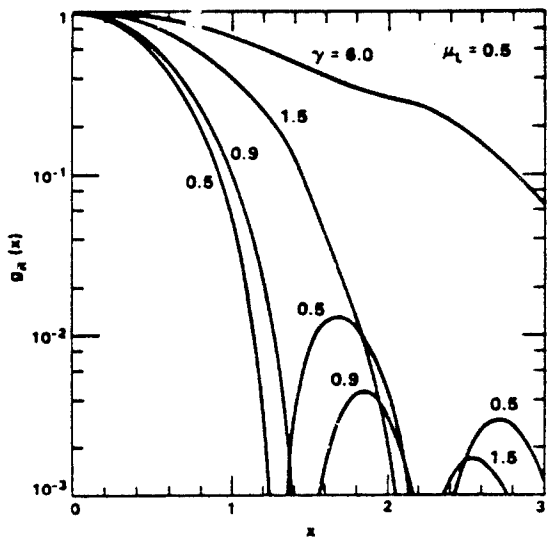

FIGURE 3. FAR-FIELD RECEIVER BEAM PATTERN $g_R(x)$ vs. NORMALIZED TRANSVERSE DISTANCE x; μ_L=0.5, AND VARIOUS γ VALUES.

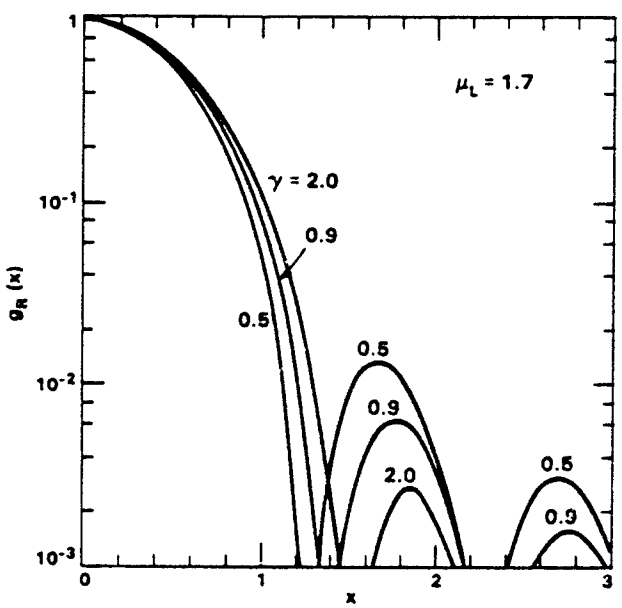

FIGURE 4. FAR-FIELD RECEIVER BEAM PATTERN $g_R(x)$ vs. NORMALIZED TRANSVERSE DISTANCE x; μ_L=1.7, AND VARIOUS γ VALUES.

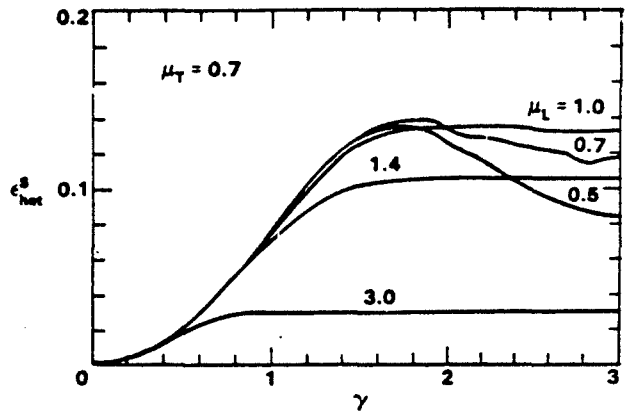

FIGURE 5. FAR-FIELD SPECKLE-TARGET MIXING EFFICIENCY $\epsilon_{het}{}^s$ vs. NORMALIZED DETECTOR DIAMETER γ FOR VARIOUS VALUES OF NORMALIZED LOCAL-OSCILLATOR INTENSITY RADIUS μ_L; μ_T=0.7.

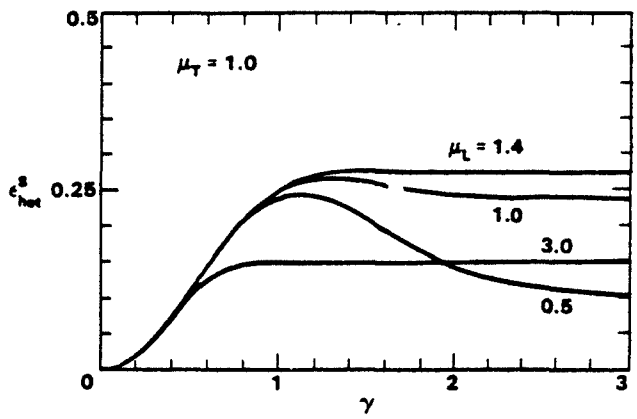

FIGURE 6. FAR-FIELD SPECKLE-TARGET MIXING EFFICIENCY $\epsilon_{het}{}^s$ vs. NORMALIZED DETECTOR DIAMETER γ FOR VARIOUS VALUES OF NORMALIZED LOCAL-OSCILLATOR INTENSITY RADIUS μ_L; μ_T=1.0.

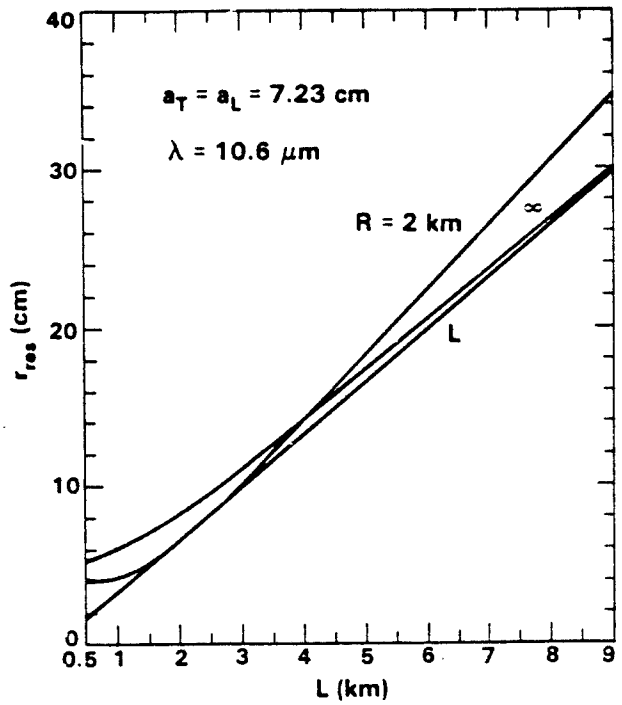

FIGURE 7. NEAR-FIELD RESOLUTION r_{res} vs. RANGE L FOR VARIOUS GEOMETRIC OPTICS FOCUS VALUES R.

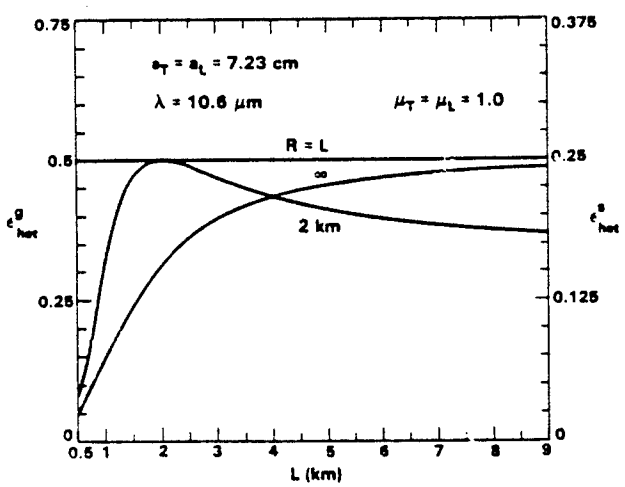

FIGURE 8. NEAR-FIELD MIXING EFFICIENCIES $\varepsilon_{het}{}^g$ AND $\varepsilon_{het}{}^s$ vs. RANGE L FOR VARIOUS GEOMETRIC OPTICS FOCUS VALUES R.

APPENDIX B

Resolution and accuracy, ambiguity and anomaly for range-spread speckle targets

Jeffrey H. Shapiro

Department of Electrical Engineering and Computer Science
Massachusetts Institute of Technology
77 Massachusetts Avenue, Cambridge, Massachusetts 02139

Abstract

Coherent laser radars used for 3-D imaging and aerosol/pollutant sensing collect target returns which comprise a range-spread speckle process. This paper addresses a class of waveform design/waveform evaluation problems for such radars. The maximum-likelihood (ML) processors and Cramer-Rao (CR) performance bounds are developed for short pulse, chirped pulse, sinusoidal amplitude-modulated pulse, and sinusoidal frequency-modulated pulse waveforms. All four of these waveforms are shown to have nearly identical ultimate range accuracies. However, range accuracy is not the only performance criterion of interest; range resolution, ambiguity, and anomaly must also be considered. Analysis and discussion of some of these aspects of waveform selection are included in the paper.

Introduction

Coherent laser radars are now being developed for a variety of imaging, detection, and remote sensing applications. In two important application areas, 3-D imaging and aerosol/pollutant sensing, the target returns comprise a range-spread speckle process. This paper addresses fundamental performance limitations, and specific performance results for targets of this class. We begin by examining the range accuracy for isolated speckle targets achievable with four prototypical pulse waveforms and maximum-likelihood (ML) processors. Cramer-Rao (CR) performance bounds are developed which show that all four of these waveforms have nearly identical ultimate range accuracies. However, in range-spread target environments range accuracy is not the only performance criterion of interest. Range resolution, which relates to the instantaneous range swath sampled by the pulse at a given time instant, is also important. In addition, range ambiguity, arising from the structure of the waveform, and range anomaly, created by noise, must also be considered. Some general features of these performance measures, as well as some specific system calculations will be presented.

Radar signal model

The model we employ in our analysis is the range-spread generalization of the model used in our previous work.[1,2] We assume a compact coherent laser radar whose operation is unaffected by atmospheric turbulence and whose intermediate-frequency (IF) received signal has complex envelope

$$\underline{r}(t) = \underline{y}(t) + \underline{n}(t), \tag{1}$$

where $\underline{y}(t)$ is the target return and $\underline{n}(t)$ is local-oscillator shot noise. The target return for a single pulse transmission obeys

$$\underline{y}(t) = E^{1/2} \int_0^\infty dz\, \underline{s}(t - 2z/c) \int d\bar{\rho}'\, \underline{T}(\bar{\rho}',z,t-z/c)\, \underline{\xi}^2(\bar{\rho}',z), \tag{2}$$

where: E is the transmitted pulse energy; $\underline{s}(t)$ is the normalized complex envelope of the transmitted pulse; $\underline{T}(\bar{\rho}',z,t)$ is the random speckle-target field reflection coefficient at transverse coordinate $\bar{\rho}'$ range z and time t; and $\underline{\xi}(\bar{\rho}',z)$ is the common normalized spatial beam pattern of transmitter and back-propagated local oscillator at range z. The shot noise $\underline{n}(t)$ is a zero-mean circulo-complex white Gaussian noise with spectral density $h\nu_0/\eta$ in terms of the photon energy and the detector quantum efficiency.

We shall assume that $\underline{T}(\bar{\rho}',z,t)$ is a circulo-complex Gaussian process with covariance function

$$\langle \underline{T}(\bar{\rho}_1',z_1,t_1)\, \underline{T}(\bar{\rho}_2',z_2,t_2)^* \rangle = \lambda^2\, T(z_1)\, \delta(\bar{\rho}_1'-\bar{\rho}_2') \cdot \delta(z_1-z_2)\, \exp[-(t_1-t_2)^2/t_c^2]. \tag{3}$$

Physically, this model corresponds to a stationary spatially-resolved speckle target with range-dependent average reflection strength $T(z)$ and coherence time t_c. For the particular case of an aerosol target we identify

$$\beta_s(\pi,z) = \pi\, T(z) \tag{4}$$

as the atmospheric backscatter coefficient ($m^{-1}\ sr^{-1}$ units) at range z, and t_c as the target-return correlation time arising from the aerosol's velocity fluctuations.

For a stationary range-spread hard target we can usually assume $t_c \to \infty$ and treat $T(z)$ as the target characteristic of interest. Note that the isolated range-L stationary hard-target model used in Refs. 1 and 2 corresponds to Eq.(3) with $t_c \to \infty$ and

$$T(z) = (\rho/\pi)\ \delta(z-L) \tag{5}$$

for ρ the target's diffuse reflectivity.

Range accuracy

Suppose the radar is used against the isolated range speckle target just described, and the IF signal for a single pulse is to be processed to yield an estimate of the range L. The maximum-likelihood range estimate, $\hat{L}_{ML}$, is the z value that maximizes[3]

$$\ell(z) = \left| \int dt\ \underline{r}(t)\ \underline{s}(t-2z/c)^* \right|^2. \tag{6}$$

Physically, this processor can be realized with a matched-filter/envelope-detector/peak detector cascade.

A range estimate $\hat{L}$ is said to be unbiased if its average value (over the shot noise and target speckle ensembles) $\langle\hat{L}\rangle$ equals the true range L, no matter what value L was. All unbiased estimates have mean-squared estimation errors that obey the Cramer-Rao inequality[3]

$$\delta\hat{L} \equiv \langle(\hat{L} - L)^2\rangle$$

$$> \frac{c^2\ (CNR + 1)\ \sigma_t^2}{8\ CNR^2\ [\sigma_t^2\ \sigma_\omega^2 - \lambda^2_{t\omega}]}. \tag{7}$$

In Eq. (7): c is the speed of light;

$$CNR = \eta E_0\ A_R\ e^{-2\beta L}\ /\ h\nu_0\ \pi L^2 \tag{8}$$

is the carrier-to-noise ratio, where β is the atmospheric extinction coefficient and

$$A_R = (\lambda L)^2\ e^{2\beta L}\ \int d\bar{\rho}\ |\ \underline{\xi}(\bar{\rho}, L)\ |^4 \tag{9}$$

is the effective heteodyne-reception area;

and

$$\sigma_t^2 = \int dt\ t^2\ |\ \underline{s}(t)\ |^2 - [\int dt\ t\ |\ \underline{s}(t)\ |^2]^2, \tag{10a}$$

$$\sigma_\omega^2 = \int dt\ |\ \dot{\underline{s}}(t)\ |^2 + [\int dt\ \dot{\underline{s}}(t)\ \underline{s}(t)^*]^2, \tag{10b}$$

$$\lambda_{t\omega} = \mathrm{Im}\ [\int dt\ \dot{\underline{s}}(t)\ \underline{s}(t)^*] + j\int dt\ t\ |\ \underline{s}(t)\ |^2 \int dt\ \dot{\underline{s}}(t)\underline{s}(t)^*, \tag{10c}$$

are parameters determined by the waveform $\underline{s}(t)$ that the radar employs. The parameters σ_t and σ_ω are the effective root-mean-square time duration and radian-frequency bandwidth of $\underline{s}(t)$, respectively. The parameter $\lambda_{t\omega}$ measures the degree of range-Doppler coupling in the waveform (see below) with $\lambda_{t\omega} = 0$ corresponding to zero coupling. Note that when $\lambda_{t\omega} = 0$ and CNR >> 1 Eq. (7) reduces to

$$\delta\hat{L} > c/2^{3/2}\ CNR^{1/2}\ \sigma_\omega, \tag{11}$$

i.e., the ultimate range accuracy goes inversely with signal bandwidth and the square root of the carrier-to-noise ratio.

Let us examine the waveform dependent factor in the CR bound, viz.

$$S = \sigma_t \,/\, [\, \sigma_t^2 \sigma_\omega^2 - \lambda_{t\omega}^2 \,]^{1/2} \tag{12}$$

for four prototypical $\underline{s}(t)$: 1) a short Gaussian pulse, 2) an upchirped/downchirped Gaussian pulse, 3) a sinusoidal amplitude-modulated (am) Gaussian pulse, and 4) a sinusoidal frequency-modulated (fm) Gaussian pulse. The specific waveforms are as follows.

Short Gaussian pulse

Here we assume

$$\underline{s}(t) = K_1 \exp\,[-(\pi W t)^2/4] \tag{13}$$

where K_1 is a normalization constant, W is the Fourier transform bandwidth (in Hz) and $4/\pi W$ is the time duration of the pulse#.

Upchirped/downchirped Gaussian pulse

In this case we assume

$$\underline{s}(t) = K_2 \exp\,[-4t^2 / T^2 - j(2\pi)^{1/2} Wt] \cdot \exp\,[j2\pi Wt\,|\,t\,|\,/T], \tag{14}$$

where T is the time duration, W is the chirp bandwidth, and WT >> 1. Note that we have chosen the upchirped/downchirped waveform to avoid the very strong range-Doppler coupling in the ordinary chirped pulse. The latter causes significant problems for non-stationary targets whose range and Doppler shift must be estimated from a single pulse.

Sinusoidal am pulse

In this case we assume

$$\underline{s}(t) = K_3 \exp\,[-4t^2 / T^2\,]\,[1 + m\cos(\pi W t)], \tag{15}$$

where T is the pulse duration, m is the modulation strength, W is the modulation bandwidth, and WT >> 1.

Sinusoidal fm pulse

Here we assume

$$\underline{s}(t) = K_4 \exp\,[-4t^2 / T^2 + j\pi(W/\omega_s)\cos(\omega_s t)\,], \tag{16}$$

where T is the pulse duration, W is the full width of instantaneous-frequency swing, ω_s is the sinusoidal modulation radian frequency, and WT >> 1, $\omega_s T$ >> 1.

S-factor value

All four of the preceding waveforms have the same nominal bandwidth W, and the last three have the same nominal time duration T. Thus, by comparing the values these waveforms yield for S in Eq. (12) we can see how their ultimate range accuracies, i.e., their respective CR bounds, compare. We find that

$$SW = \begin{cases} 2/\pi = 0.64, & \text{short pulse} \\ (\pi^2/2 - 1)^{-1/2} = 0.50, & \text{chirped pulse} \\ (2 + m^2)^{1/2}/m\pi = 0.55, & \text{for } m=1, \text{ am pulse} \\ 2^{1/2}/\pi = 0.45, & \text{fm pulse.} \end{cases} \tag{17}$$

For the pure Gaussian cases, bandwidth and time duration are measured full width to e^{-2} intensity points.

(Our choice of m=1 for the am pulse is dictated by the desire for envelope detector compatibility). It is apparent from these numbers that all four waveforms have nearly identical range accuracies. Accordingly, the accuracy achievable with ML processing cannot serve as a reason for choosing one waveform over another.

Range resolution

A second waveform performance criterion of interest is its range resolution z_{RES}. Roughly speaking, z_{RES} is the range swath which can give rise to a target return at some particular time, e.g., from (2) it follows that $z_{RES} = cT/2$ for a rectangular pulse of duration T. Range resolution plays a role in distinguishing discrete targets located at various ranges from the radar. For range-spread targets such as aersols, z_{RES} is the range swath over which the backscatter profile is smeared. Finally, as will be discussed later, range resolution enters into the anomaly calculation.

To illustrate the behavior of z_{RES} mentioned above, consider the case of aerosol sensing using the chirped Gaussian pulse

$$\underline{s}(t) = K \exp\left[-4t^2 / T^2 - j\pi W t^2 / T\right], \tag{18}$$

which has duration T and chirp bandwidth W, with WT >> 1 assumed. We shall assume far-field propagation using a collimated Gaussian-beam transmitter/local oscillator beam of initial e^{-2} intensity radius a. We shall also assume matched-filter/envelope-detection is performed for range z, i.e., the receiver generates $\ell(z)$ given by (6). It follows that the carrier-to-noise ratio for range z can be written in the form

$$CNR(z) = \int_0^\infty dz'\, Q(z')\, F(z-z'), \tag{19}$$

where

$$Q(z) = \left[\eta\, E\, c\, T\, \pi^{3/2}\, a^2\, \beta_s(\pi,Z)/h\nu_0\, 4z^2\right] \exp\left[-2 \int_0^z \beta(z')\, dz'\right] \tag{20}$$

is the infinite resolution aerosol-return CNR profile, and

$$F(z) = g(\pi\, z_{RES}^2 / 8)^{-1/2} \exp\left(-8\, z^2/z_{RES}^2\right) \tag{21}$$

is the effective probe function of the chirped-transmitter/matched-filter receiver.

In Eq. (21) the range resolution is given by

$$z_{RES} = \frac{cT/2^{1/2}}{\left[1 + (\pi WT/4)^2 / (1 + T^2/4t_c^2)\right]^{1/2}}, \tag{22}$$

$$g = \int dz\, F(z) = \left[1 + T^2/4t_c^2 + (\pi WT/4)^2\right]^{-1/2}. \tag{23}$$

For example, suppose T = 10μs, W = 20MHz and t_c = 1μs; we find that z_{RES} = 68.8m. Were there no aerosol decorrelation, i.e., $t_c \to \infty$, these same T and W values yield much better resolution, z_{RES} = 13.5m. On the other hand, for a smoothly varying aerosol distribution,

$$CNR(z) = Q(z)\, g \tag{24}$$

and g varies by less than 0.1% for T and W as above when t_c changes from infinity down to 1μs. Physically, when $t_c < \infty$ the loss of correlation over the pulse duration T spoils the resolution by spoiling the pulse-compression in the matched filter. Yet, because the broadened probe function now collects aerosol returns from a larger range swath, there is almost no immediate loss in CNR.

Range ambiguity

The discussion thus far of range accuracy and range resolution presumes that in any problem there is a single range interval of interest. In particular, in the accuracy work we were interested in an interval of width $2\Delta L$ about L, and in the resolution work we were interested in an interval of width z_{RES} about z. Many radar waveforms have range ambiguities, i.e., for a target at range L there are a variety of z values which yield nearly identical noise-free matched-filter aspects outputs.

$$\ell_0(z) = \left| \int dt\, \underline{s}(t-2L/c)\, \underline{s}\,(t-2z/c)^* \right|^2. \tag{25}$$

Because of noise effects, the radar will be hard pressed to correctly sort out which of these ambiguous range values to associate with the target. In this regard the sinusoidal am and fm pulses we considered under range accuracy are at a disadvantage with respect to the short pulse and chirped pulse waveforms considered therein. For the sinusoidal am pulse we have

$$\ell_0(L-ck/W) = \exp(-16\ k^2/W^2\ T^2) \tag{26}$$

for k an integer, which implies, because WT >> 1, range ambiguities exist every c/W. Likewise, for the sinusoidal fm pulse and k an integer we obtain

$$\ell_0(L - \pi kc/\omega_s) = \exp\ (-16\pi^2\ k^2/\omega_s^2\ T^2), \tag{27}$$

implying range ambiguities every $\pi c/\omega_s$, as $\omega_s T >> 1$.

Range anomaly

Even when the radar's waveform $\underline{s}(t)$ is not prone to range ambiguity, a single-pulse range estimate from a speckle target will not have an accuracy well approximated by the CR bound (7). Indeed, the range estimate may be anomalous, i.e., it may lie outside of the z_{RES} interval that contains the target. This is the well known threshold problem in nonlinear estimation theory[4]. Physically, a single-pulse speckle target return may, owing to destructive interference, be weak enough that the ML processor chooses a range estimate corresponding to a noise peak that may be arbitrarily far removed from the correct range-resolution interval. For an a priori target range uncertainty region of width

$$\Delta z = M\ z_{RES} \tag{28}$$

no Doppler uncertainty, and a radar waveform without ambiguity problems the probability of range anomaly on a single pulse is approximately[3]

$$Pr(A) = [\ln M - (2M)^{-1} + 0.577]\ /CNR. \tag{29}$$

Because the root-mean-square range estimation error given a range anomaly has occurred is roughly $\Delta z/6^{1/2}$, the single-pulse range accuracy is actually dominated by these events, i.e., $Pr(A)\ \Delta z/6^{1/2}$ typically exceeds the CR bound (7).

In order to circumvent the anomaly problem, a sequence of N independent pulses can be employed. The anomaly probability now becomes

$$Pr(A) = M\ (1+CNR)^N/(\pi N)^{1/2}\ CNR\ (1+CNR/2)^{2N-1}; \tag{30}$$

it follows for reasonable N and CNR values that N-pulse range accuracy can approach the N-pulse CR bound

$$\delta L = c\ S\ (CNR + 1)^{1/2}\ /\ 8^{3/2}\ CNR\ N^{1/2}. \tag{31}$$

Acknowledgements

This research was supported by the Department of the Air Force. The U.S. Government assumes no responsibility for the information presented.

References

1. J. H. Shapiro, B. A. Capron and R. C. Harney, "Imaging and Target Detection with a Heterodyne-Reception Optical Radar", Appl. Opt., Vol. 20, pp. 3292-3313, 1981.

2. D. M. Papurt, J. H. Shapiro and R. C. Harney, "Atmospheric Propagation Effects on Coherent Laser Radars," Proc. SPIE, Vol. 300, pp. 86-99, 1981.

3. H. L. Van Trees, Detection, Estimation, and Modulation Theory, Part III, Wiley, New York,, 1971, Chap. 10.

4. H. L. Van Trees, Detection, Estimation, and Modulation Theory, Part I, Wiley, New York 1968, Chap. 4.

APPENDIX C

PERFORMANCE ANALYSES FOR DOPPLER AND CHIRPED LASER RADARS*

22 September 1983

J. H. Shapiro and P. L. Mesite
Massachusetts Institute of Technology
Department of Electrical Engineering and Computer Science
Cambridge, Massachusetts 02139

ABSTRACT

Two laser radar signal models are developed, one for a Doppler-shifted target return with randomly time-dependent speckle and short-term laser frequency instability, and one for a clutter return with the above characteristics augmented by a random macro-motion Doppler shift. Target-return velocity resolution for a Doppler radar, and target-return range resolution for a chirped radar are derived from the former model. Clutter-limited false alarm probabilities are derived from the latter. Experimental Doppler-radar returns from a moving flame-sprayed aluminum calibration plate are analyzed for comparison with the target speckle model. Experimental Doppler-radar tree clutter returns are analyzed for comparison with the clutter model.

1.0 INTRODUCTION

Velocity-imaging Doppler laser radars, and range-imaging laser radars which use high time-bandwidth (TW) product waveforms, both employ pixel dwell times far in excess of the pulse durations of pulsed-imager laser radars. The long dwell times make the performance of the former systems subject to degradations arising from laser frequency instability and target decorrelation to which the latter systems are largely immune. These degradations must be included, along with speckle effects and, for Doppler radars, clutter, in analyses of resolution and signal-to-noise ratio for such systems. In this paper, preliminary models for the preceding effects and resulting performance analyses are presented. Data collected with the MIT Lincoln Laboratory Doppler radar are used to test some of the speckle and clutter characteristics assumed in the models.

Section 2.0 presents the radar system structure to be analyzed and develops two radar signal models. The first model describes a Doppler-shifted target return with randomly time-dependent speckle and short-term laser frequency

*This work was supported by the Department of the Air Force Contract F19628-80-C-0002 and the U.S. Army Research Office Contract DAAG29-80-K-0032. "The U.S. Government assumes no responsibility for the information presented."

instability. The second model characterizes a clutter return with the above features augmented by a random macro-motion Doppler shift. Performance analyses using these models are given in Section 3.0. Velocity resolution for a Doppler radar, and range resolution for a chirped radar are derived from the target return model. Clutter-limited false alarm probabilities are derived from the clutter model. Section 4.0 uses experimental results to examine the validity of the models. Spatially averaged intensity histograms of experimental Doppler-radar returns from a moving flame-sprayed aluminum calibration plate are analyzed for comparison with accepted speckle behavior. Velocity histograms of experimental tree clutter are analyzed for comparison with the assumed clutter model.

2.0 SYSTEM MODELS

The basic system structure we shall assume is shown schematically in Fig. 1. It is a monostatic shared-optics coherent laser radar using a single laser for both the transmitter and local oscillator functions. Long dwell time operation without transmitter modulation is used for velocity-imaging operation. Long dwell time operation with a chirped (internally or externally modulated) transmitter is used for range-imaging operation. In either case, an externally generated frequency offset is used to obtain the local oscillator beam for unaliased heterodyne detection of the radar return.

As in our earlier studies[1,2,3,4] the fundamental quantity of interest is the complex envelope of the intermediate-frequency (IF) received signal for a single pixel dwell time, given by

$$\underline{r}(t) = \underline{y}(t) + \underline{n}(t) \qquad (1)$$

---

1. Shapiro, J. H., Capron, B. A., and Harney, R. C., "Imaging and Target Detection with a Heterodyne-Reception Optical Radar," Appl. Opt. 20, 3292-3313 (1981).

2. Papurt, D. M., Shapiro, J. H., and Harney, R. C., "Atmospheric Propagation Effects on Coherent Laser Radars," Proc. SPIE 300, 86-99 (1981).

3. Papurt, D. M., Shapiro, J. H., and Lau, S. T., "Measured Turbulence and Speckle Effects in Laser Radar Target Returns," Proc. SPIE 415, in press (1983).

4. Shapiro, J. H., "Resolution and Accuracy, Ambiguity and Anomaly for Range-Spread Speckle Targets," Proc. SPIE 415, in press (1983).

in terms of the radar return $\underline{y}(t)$ and the local oscillator shot noise $\underline{n}(t)$. The excellent spatial resolution of laser radar equipment makes it reasonable to assume that $\underline{y}(t)$ is either a target return or a clutter return, but not a combination of the two.[5] The local-oscillator shot noise $\underline{n}(t)$ is a zero-mean circulo-complex white Gaussian noise process of spectral height $h\nu_0/\eta$ for $h\nu_0$ the photon energy at the laser wavelength and η the quantum efficiency of the photodetector.

2.1 TARGET-RETURN MODEL

We assume a compact coherent laser radar whose operation is unaffected by atmospheric turbulence, but is subject to atmospheric extinction with coefficient $\alpha\ m^{-1}$. A range-spread, Doppler-shifted, time-dependent speckle target will then give rise to a single pixel target return complex envelope[4]

$$\underline{y}(t) = E^{1/2} \exp(j2\pi f_D t) \int_0^\infty dz\ \underline{s}(t-2z/c) \exp[-j(\phi(t-2z/c)-\phi(t))]$$

$$\cdot \int d\bar{\rho}\ \underline{I}(\bar{\rho},z,t-z/c)\ e^{-\alpha z}\ \underline{\xi}^2(\bar{\rho},z). \qquad (2)$$

In Eq. (2): E is the energy transmitted during the dwell time; $f_D = 2v_z/\lambda$ is the Doppler frequency shift associated with the nominal longitudinal target velocity v_z at the radar wavelength λ; $\underline{s}(t)$ is the normalized complex envelope of the transmitted field neglecting frequency instability effects; $\phi(t)$ is the random phase shift of the transmitted field that is due to laser frequency instability; $\underline{I}(\bar{\rho}, z, t)$ is the random speckle-target field reflection coefficient (neglecting the net Doppler shift f_D) at transverse coordinate $\bar{\rho} = (x,y)$ range z and time t; and $\underline{\xi}(\bar{\rho},z)$ is the common normalized free-space spatial beam of the transmitter and local oscillator at range z.[6]

For velocity imaging we shall take $\underline{s}(t)$ to be a transform limited Gaussian pulse

$$\underline{s}(t) = (8/\pi T^2)^{1/4} \exp(-4t^2/T^2), \qquad (3)$$

---

5. Harney, R. C., "Design Considerations for the Infrared Airborne Radar (IRAR) MTI Subsystem," Project Report TST-26, Lincoln Laboratory, M.I.T. (July 1980).

6. The assumption of common beam patterns has been made for simplicity. An examination of transmitter and local-oscillator beam pattern effects on the spatial resolution and heterodyne mixing efficiency of a monostatic radar is given in Shapiro, J. H., Dardzinski, V. E., and Tung, E. W., "Coherent Laser Radar Antenna Patterns and Mixing Efficiencies," Active Systems Specialty Group, IRIS (November 1983).

whose dwell time (full width to e^{-2} points of $|\underline{s}(t)|^2$) T is tens of μsec to provide satisfactory Doppler resolution. In this case it is reasonable to assume that the target is unresolved in range, viz. $\underline{I}(\bar{\rho},z,t)$ in Eq. (2) is a zero-mean circulo-complex Gaussian process with covariance function

$$\langle \underline{I}(\bar{\rho}_1,z_1,t_1)\underline{I}^*(\bar{\rho}_2,z_2,t_2)\rangle = (\lambda^2 \rho/\pi)$$

$$\cdot\delta(\bar{\rho}_1-\bar{\rho}_2)\ \delta(z_1-z_2)\ \delta(z_1-L)$$

$$\cdot\exp[-(t_1-t_2)^2/t_c^2]. \qquad (4)$$

Here ρ is the (assumed uniform) diffuse reflectivity of the target, L is the nominal target range, and t_c is the coherence time of the target's speckle process.

For range imaging we shall assume $f_D = 0$ to avoid range/Doppler ambiguity[7], and take $\underline{s}(t)$ to be the chirped Gaussian pulse

$$\underline{s}(t) = (8/\pi T^2)^{1/4} \exp[-4t^2/T^2 - j\pi W t^2/T] \qquad (5)$$

of duration T and chirp bandwidth W, with TW>>1. In this case the target may be resolved in range, so we modify (4) to become

$$\langle \underline{I}(\bar{\rho}_1,z_1,t_1)\ \underline{I}^*(\bar{\rho}_2,z_2,t_2)\rangle = \lambda^2 T(z_1)$$

$$\cdot\delta(\bar{\rho}_1-\bar{\rho}_2)\ \delta(z_1-z_2)\ \exp[-(t_1-t_2)^2/t_c^2], \qquad (6)$$

in terms of the range-dependent average reflection strength $T(z)$. For the important example of an aerosol target we identify

$$\beta_s(\pi,z) = \pi T(z) \qquad (7)$$

as the atmospheric backscatter coefficient (m^{-1} sr^{-1} units) at range z.

---

7. In real chirped systems the range/Doppler ambiguity can be resolved by using a composite waveform consisting of an up-chirp segment and a down-chirp segment, see, e.g., Skolnik, M. I., Introduction to Radar Systems (McGraw-Hill, New York, 1980), pp. 81-92.

It still remains for us to characterize the frequency instability term $\exp[-j(\phi(t-2z/c)-\phi(t))]$ appearing in Eq. (2), which is an effect not previously treated in our pulsed imager work.[1,2,3] Physically, this term arises from the beat between the range delayed random phase shift of the transmitter beam and the undelayed random phase shift from the same laser used as the local oscillator. Typical CO_2 lasers used in coherent laser radars have very narrow short-term linewidths with slowly (and randomly) varying center frequencies that lead to appreciably larger long-term linewidths. To model this behavior we shall write the random phase process as

$$\phi(t) = 2\pi \int_{-\infty}^{t} f_I(\tau)d\tau \tag{8}$$

in terms of an instantaneous frequency $f_I(t)$ that is a zero-mean stationary Gaussian random process with covariance function

$$\langle f_I(t+\tau)f_I(t)\rangle = \sigma_f^2 \exp(-|\tau|/t_f). \tag{9}$$

In this formulation, σ_f is the root-mean-square (rms) long-term laser bandwidth, and $1/\pi t_f$ gives the 3dB short-term laser bandwidth, where $\sigma_f t_f >> 1$ is assumed.

From Eqs. (8) and (9) it is a straightforward but tedious calculation to compute the mean function and correlation function of the frequency instability term for range z

$$\underline{w}_z(t) \equiv \exp[-j(\phi(t-2z/c) - \phi(t))]. \tag{10}$$

Of particular interest are the following approximate results for the spectral density of $\underline{w}_z(t)$

$$S_{ww}(f) \equiv \int_{-\infty}^{\infty} d\tau \, \langle \underline{w}_z(t+\tau)\underline{w}_z^*(t)\rangle \, e^{-j2\pi f\tau}$$

$$= \begin{cases} [1 - (4\pi\sigma_f z/c)^2]\,\delta(f) + \dfrac{2t_f(4\pi\sigma_f z/c)^2}{(2\pi f t_f)^2 + 1}, & \text{for } 2\sigma_f z/c \ll 1, \quad (11a) \\[2ex] \left(\dfrac{ct_f}{8\pi\sigma_f{}^2 z}\right)^{1/2} \exp\left(-\dfrac{f^2 ct_f}{8\sigma_f{}^2 z}\right), & \text{for } 2z/ct_f \ll 1,\ 2\sigma_f z/c \gg 1, \quad (11b) \\[2ex] (4\pi\sigma_f{}^2)^{-1/2} \exp\,(-f^2/4\sigma_f{}^2), & \text{for } 2z/ct_f \gg 1, \quad (11c) \end{cases}$$

which have been plotted in Fig. 2. Equation (11a) applies when the 2z/c sec propagation delay is insufficient to resolve the long-term laser linewidth; the resulting spectrum comprises a spike plus a Lorentzian of 3dB bandwidth $1/\pi t_f$. Equation (11b) corresponds to the normal operating regime for laser radars in which the propagation delay resolves the long-term linewidth but not the short-term linewidth; here the spectrum is Gaussian with rms bandwidth $2\sigma_f(z/ct_f)^{1/2}$, which is much broader than $1/\pi t_f$ but much narrower than σ_f. Finally, Eq. (11c) describes very long path operation for which the propagation delay resolves the short-term linewidth; here the spectrum is Gaussian with rms bandwidth $2^{1/2}\sigma_f$ because the delayed transmitter beam has a frequency instability that is statistically independent of that of the local oscillator.

2.2 CLUTTER-RETURN MODEL

An important consideration in assessing the utility of a Doppler radar as a moving target indication (MTI) system is its ability to distinguish a slowly moving hard target from background clutter returns caused by windblown trees, etc.[5] Equations (1) and (2) are valid for background clutter, with $\underline{I}(\bar{\rho}, z, t)$ now being the complex field reflection coefficient of the clutter at transverse coordinate $\bar{\rho}$, range z, and time t. For velocity imaging with the long dwell time transmitted pulse (3), we hypothesize that $\underline{I}(\bar{\rho},z,t)$ will be such that a clutter return $\underline{y}(t)$ will take the form

$$\underline{y}(t) = E_c^{1/2}\underline{s}(t-2L/c)\underline{w}_L(t)\underline{y}_c(t)\ \exp\left[j2\pi \int_{-\infty}^{t} f_c(\tau)d\tau\right], \qquad (12)$$

where E_c is the average received clutter energy, $\underline{s}(t)$ is the normalized transmitted field complex envelope neglecting frequency instability (given by Eq. (3)), L is the nominal range, and $\underline{w}_L(t)$ is the frequency instability term (given by Eq. (10)). The new features in Eq. (12) are a clutter-speckle process $\underline{y}_c(t)$, taken to be a zero-mean unity-variance stationary circulo-complex Gaussian random process with spectral density

$$S_{y_c y_c}(f) = (2\pi\sigma_c^2)^{-1/2}\ \exp\ (-f^2/2\sigma_c^2), \qquad (13)$$

and a clutter macro-motion instantaneous Doppler shift $f_c(t)$, taken to be a Gaussian random process that is statistically independent of $\underline{y}_c(t)$ with mean m_{fc}, variance σ_{fc}^2, and correlation time far in excess of the pixel dwell time T.

Physically, Eq. (12) treats the clutter return as being unresolved in range coming from reflectors located L m in front of the radar. The $\underline{y}_c(t)$ process represents micro-motion, i.e., rapid intra-pixel variations, of the clutter reflectors. The $f_c(t)$ process represents macro-motion, i.e., slow gross-pixel movement, of the clutter reflectors. The combination of these two processes

$$\underline{\tilde{y}}(t) \equiv \underline{y}_c(t)\exp\left[j2\pi \int_{-\infty}^{t} f_c(\tau)d\tau\right], \qquad (14)$$

can be shown to have a spectrum

$$S_{\tilde{y}\tilde{y}}(f) = (2\pi\sigma^2)^{-1/2}\exp[-(f-m_{fc})^2/2\sigma^2], \qquad (15)$$

whose mas width is

$$\sigma = (\sigma_c^2 + \sigma_{fc}^2)^{1/2}. \qquad (16)$$

Thus, the long-term bandwidth of our clutter model is a composite of micro-motion and macro-motion contributions.

3.0 PERFORMANCE ANALYSES

In this section we shall apply the models presented above to a variety of radar performance calculations. These calculations will illustrate the interplay of speckle, frequency instability, and clutter effects.

3.1 VELOCITY IMAGING

Consider a single-pixel velocity-imaging radar return modeled by Eqs. (1)-(4), (8)-(10), (11b). Let us assume that the target range L is known, and that a surface acoustic wave (SAW) Fourier transform device/envelope detector combination[8] is used to obtain the processed signal

$$R(f) = \left|\int dt\ \underline{s}^*(t-2L/c)\underline{r}(t)e^{-j2\pi ft}\right|^2. \tag{17}$$

Typically, R(f) is peak detected, i.e., f^0 for which $\max_f R(f) = R(f^0) \equiv R^0$ is found; the radar then assigns the velocity value $v_z{}^0 = \lambda f^0/2$ and the intensity value R^0 to this pixel[9]. Here, we shall study the velocity resolution, carrier-to-noise ratio (CNR), and signal-to-noise ratio (SNR) behavior[10] of the processed signal R(f).

The mean value <R(f)> of the processed signal consists of a target-return contribution

$$\left\langle\left|\int dt\ \underline{s}^*(t-2L/c)\underline{y}(t)e^{-j2\pi ft}\right|^2\right\rangle =$$

$$\frac{E(\lambda^2\rho/\pi)\int d\bar{\rho}\left|\underline{\xi}(\bar{\rho},L)\right|^4 e^{-2\alpha L}2^{5/2}\ \exp[-8(f-f_D)^2/f_{RES}{}^2]}{\pi^{1/2}f_{RES}}, \tag{18}$$

where

$$f_{RES} = (2^{5/2}/\pi T)[1+(\pi\sigma_f T)^2 2L/ct_f + T^2/4t_c{}^2]^{1/2}, \tag{19}$$

plus a noise contribution

$$\left\langle\left|\int dt\ \underline{s}^*(t-2L/c)\underline{n}(t)e^{-j2\pi ft}\right|^2\right\rangle = h\nu_0/n. \tag{20}$$

Physically, f_{RES} is the full width between the e^{-2} attenuation points of the target-return contribution to <R(f)>. Thus,

$$v_{RES} = \lambda f_{RES}/2 \tag{21}$$

---

8. Arsenault, D. R., and Dolat, V. S., "Compact Multiple-Channel SAW Sliding-Window Spectrum Analyzer," 1981 Ultrasonics Symposium (IEEE, New York, 1981), pp. 220-225.

9. Biron, D. G., and Edwards, B. E., "Moving Target Imaging Radar Utilizing Both Intensity and Velocity Information," CLEO '82 Technical Digest (Opt. Soc. of America, Washington, D.C., 1982), pp. 128-129.

10. As elaborated in Ref. 1., CNR measures the relative strength of the target return and noise at the input to the IF signal processor, and SNR measures the relative strength of the mean target-return and fluctuations at the output of the signal processor.

is the velocity resolution of the radar as set by the pixel dwell time (T), frequency instability ($2\sigma_f^2 L/ct_f$), and target decorrelation (t_c) effects. In Fig. 3 we have plotted v_{RES} vs.target correlation time t_c for T = 20 μsec (corresponding to dwell-time limited resolution of 1.72 km/h = 0.48 m/s), assuming no frequency instability ($2\sigma_f^2 L/ct_f = 0$). This figure shows that appreciable resolution loss occurs for correlation times shorter than 10 μsec, such as typically occur with aerosol targets. In Fig. 4 we have plotted v_{RES} vs. target range L for T=20 μsec, and four pair of σ_f, t_f values, assuming no target decorrelation ($t_c \to \infty$). Here we see that the dwell time is sufficiently short that severe resolution loss occurs only under extreme (σ_f=200kHz, $t_f = 10^{-4}$ sec) instability conditions.

The CNR at frequency f is defined to be the ratio of the signal contribution to <R(f)> to the noise contribution to <R(f)>. At the target Doppler shift f_D we have that

$$\mathrm{CNR} = \frac{\eta E(\lambda^2\rho/\pi)\int d\bar{\rho}\left|\underline{\xi}(\bar{\rho},L)\right|^4 e^{-2\alpha L}\, 2^{5/2}}{h\nu_0 \pi T f_{RES}}. \tag{22}$$

Equation (22) can be recast into the more familiar form[6,11]

$$\mathrm{CNR} = \frac{\eta P_T}{h\nu_0 B}\,\frac{\rho A_R^S}{\pi L^2}\, e^{-2\alpha L}\,\frac{2^{5/2}}{\pi T f_{RES}} \tag{23}$$

in terms of the transmitter peak power P_T, an effective pulse bandwidth $B \equiv P_T/E$, and the effective heterodyne detection mixing area A_R^S. From (19) we see the final fraction on the right in (23) represents a CNR loss that is due to frequency spreading of the target return. This loss will be significant whenever v_{RES} is appreciably worse than the 1.72 km/h dwell-time limited value.

The SNR at frequency f is defined to be

$$\mathrm{SNR} = (\langle R(f)\rangle - h\nu_0/\eta)^2/\mathrm{var}(R(f)), \tag{24}$$

i.e., it is the ratio of the squared mean target-return contribution to R(f) to

---

11. Shapiro, J. H., "Target-Reflectivity Theory for Coherent Laser Radars," Appl. Opt. 21, 3398-3407 (1982).

the variance of $R(f)$, where the latter includes target-return and noise fluctuations. Equation (24) can be put into the standard form[1]

$$SNR = \frac{CNR/2}{1 + CNR/2SNR_{sat} + (2CNR)^{-1}} \tag{25}$$

in terms of the CNR and the saturation signal-to-noise ratio

$$SNR_{sat} \equiv \langle R_y(f)\rangle^2/var(R_y(f)), \tag{26}$$

where

$$R_y(f) = \left|\int dt\ \underline{s}^*(t-2L/c)\underline{y}(t)\ e^{-j2\pi ft}\right|^2 \tag{27}$$

is the target-return component of $R(f)$. Equation (25) implies that SNR reaches the limiting value SNR_{sat}, arising from target-return fluctuations, when $CNR \gg \max(5, 2SNR_{sat})$. After some tedious algebra we find that the saturation signal-to-noise ratio at frequency f_D obeys

$$SNR_{sat} = \{2f_{RES}^2/f'_{RES}f''_{RES} - 1\}^{-1}, \tag{28}$$

where f'_{RES} is obtained from the right side of (19) with $L=0$ and f''_{RES} is obtained from the right side of (19) with L replaced by 2L. When frequency instability effects are insignificant (as is true for most of the Fig. 4 parameters), (28) reduces to the well-known unity saturation signal-to-noise ratio of laser speckle. However, when the frequency instability term dominates (19), Eq. (28) yields a value much less than unity, indicating worse than speckle target-return fluctuations.

3.2 RANGE IMAGING

Now let us consider a single-pixel range-imaging radar return modeled by Eqs. (1), (2), (5), (6), (8) - (10), (11b). Here we assume that a SAW pulse compressor is used to obtain the processed signal[4]

$$\ell(z) = \left|\int dt\ \underline{s}^*(t-2z/c)\underline{r}(t)\right|^2. \tag{29}$$

Typically, $\ell(z)$ is peak detected, i.e., z^o for which $\max_z \ell(z) = \ell(z^o) \equiv \ell^o$ is found; the radar then assigns the range value z^o and the intensity value ℓ^o to this pixel. Once again we shall be interested in the resolution, CNR, and SNR of the processed signal; the development parallels that just presented for velocity imaging.

The average target-return contribution to the processed signal is

$$\langle \ell_y(z) \rangle = \int_0^\infty dz'\ Q(z')\ F(z-z';z'), \tag{30}$$

where

$$\ell_y(z) = \left| \int dt\ \underline{s}^*(t-2z/c)\underline{r}(t) \right|^2, \tag{31}$$

$$Q(z) = E(\lambda^2 \pi^{1/2}/4) \int d\bar{\rho} \left| \underline{\xi}(\bar{\rho},z) \right|^4 cTe^{-2\alpha z}\, T(z), \tag{32}$$

is the infinite resolution average target-returr profile, and

$$F(z;z') = g(8/\pi z_{RES}{}^2)^{1/2} \exp\ (-8z^2/z_{RES}{}^2), \tag{33}$$

with

$$z_{RES} = \frac{cT/2^{1/2}}{[1+(\pi WT/4)^2/(1+(\pi\sigma_f T)^2 2z'/ct_f + T^2/4t_c{}^2)]^{1/2}}, \tag{34}$$

and

$$g = \int dz F(z;z') =$$

$$[1+(\pi\sigma_f T)^2 2z'/ct_f + T^2/4t_c{}^2 + (\pi WT/4)^2]^{-1/2}, \tag{35}$$

is the effective range probe function of the radar. Equations (30) - (34) imply that z_{RES} is the range resolution of the radar at range z', i.e., it is the full width in the z coordinate between the e^{-2} attenuation points of F(z;z'). Note that z_{RES} includes frequency instability and target decorrelation effects in addition to its chirp duration and chirp bandwidth dependence. Under typical operating conditions, the target range profile $T(z)$ may be appreciably narrower than the nominal target range L. In this case, which we shall employ in what follows, we may set z' = L in (34) and (35). To exhibit the effect of target decorrelation on range resolution, we have plotted z_{RES} vs. t_c in Fig. 5, with T = 10 μsec and W = 20 MHz (corresponding to a chirp-bandwidth limited resolution of 13.5m) assuming no frequency instability. Here we see the same resolution loss that transpired for the Doppler radar in Fig. 3, viz., z_{RES} degrades rapidly for t_c <10μsec. In Fig. 6 we have plotted z_{RES} vs. target range L for T = 10 μsec, W = 20 MHz, and three pair of σ_f, t_f values,

assuming no target decorrelation. As was seen in Fig. 4 for velocity resolution, only extreme instability conditions cause a major range resolution loss.

The CNR at range z is defined to be the ratio of $\langle \ell_y(z) \rangle$, the signal contribution to $\langle \ell(z) \rangle$, to $h\nu_0/\eta$, the noise contribution to $\langle \ell(z) \rangle$. At the nominal target range L we have that

$$\mathrm{CNR} = (\eta/h\nu_0)\int_0^\infty dz'\; Q(z')\; F(L-z';L)$$

$$= \begin{cases} \dfrac{\eta P_T}{h\nu_0 B}\;\dfrac{\rho A_R^S}{\pi L^2}\; e^{-2\alpha L}\; L_{hard}, & \text{(36a)} \\ \text{for a "hard" target obeying (4),} \\ \dfrac{\eta P_T}{h\nu_0 B}\;\dfrac{\beta_s(\pi,L)z'_{RES}\hat{A}_R^S}{\pi L^2}\; e^{-2\alpha L}\; L_{soft}, & \text{(36b)} \\ \text{for a "soft" (aerosol) target obeying (7),} \end{cases}$$

where P_T is the transmitter peak power, $B \equiv P_T/E$ is an effective pulse bandwidth, A_R^S is the effective heterodyne mixing area[6], and

$$L_{hard} = gcT/2^{1/2}z_{RES}, \tag{37}$$

$$z'_{RES} = cT\pi^{1/2}/4[1+(\pi WT/4)^2]^{1/2}, \tag{38}$$

$$L_{soft} = gcT\pi^{1/2}/4z'_{RES}. \tag{39}$$

Equations (36a) and (37) show that the CNR obtained from a hard target, i.e., one that is unresolved in range, takes the form of the standard monostatic radar equation times the loss factor L_{hard}. Via (34) and (35) it is easily shown that

$$L_{hard} = [1+(\pi\sigma_f T)^2 2L/ct_f + T^2/4t_c^2]^{-1/2}, \tag{40}$$

which implies $L_{hard} \leq 1$ with $L_{hard} = 1$ whenever z_{RES} is approximately equal to its chirp-bandwidth limited value. The hard target loss factor is similar to the Doppler radar loss factor encountered in Eq. (23); somewhat different

behavior is seen in the soft target case. Equation (36b) is basically the usual aerosol monostatic radar equation times the loss factor L_{soft}, which we have plotted in Fig. 7 vs. t_c for T = 10μsec and W = 20 MHz assuming no frequency instability. Comparing Figs. 5 and 6, we see that for aerosol targets substantial resolution is lost before any perceptible drop in CNR occurs. The reason for this disparity is that resolution degrades as the effective probe function F broadens due to loss of coherence, but as this broadening occurs the radar collects aerosol returns from a larger range swath, so there is almost no immediate reduction in CNR.

The SNR at range z is defined to be the ratio of the squared mean target-return contribution to $\ell(z)$ to the variance of $\ell(z)$, and obeys (25) with CNR from (36) and

$$SNR_{sat} \equiv \langle \ell_y(z) \rangle^2 / var(\ell_y(z)) \tag{41}$$

giving the limiting SNR value set by target-return fluctuations. We shall not give explicit results for SNR_{sat}; it is sufficient to note (cf. (28)) that $SNR_{sat} \leq 1$ with equality when frequency instability effects are insignificant.

3.3 CLUTTER-LIMITED FALSE ALARM PROBABILITY

In this section we shall study the clutter-limited false alarm probability of the Doppler radar whose single-pixel velocity-imaging performance was addressed in Section 3.1. Here we shall consider the following idealized single-pixel target detection problem[1]. For a particular range L, and Doppler frequency f_D, the processed signal $R(f_D)$ defined in (17) comprises either clutter-return plus noise (hypothesis H_0) or target-return plus noise (hypothesis H_1). For simplicity, we shall assume that target decorrelation and frequency instability effects are negligible on the target return, and frequency instability effects are insignificant on the clutter return. The radar receiver will use the threshold detection rule

$$R(f_D) \underset{\text{say } H_0}{\overset{\text{say } H_1}{\gtrless}} \gamma \tag{42}$$

to decide on the absence or presence of a moving target at range L velocity $\lambda f_D/2$ given the observation $R(f_D)$. Three performance quantities of interest are the noise-limited false alarm probability

$$P_F = \Pr[R(f_D) \geq \gamma | \underline{r}(t) = \text{noise}], \tag{43}$$

the clutter-limited false alarm probability

$$P_{Fc} = \Pr[R(f_D) \geq \gamma | \underline{r}(t) = \text{clutter} + \text{noise}], \tag{44}$$

and the detection probability

$$P_D = \Pr[R(f_D) \geq \gamma | \underline{r}(t) = \text{target} + \text{noise}]. \tag{45}$$

Ideally, we want to achieve $P_F = P_{Fc} = 0$ and $P_D = 1$, but because of noise $0 < P_F$ and $P_D < 1$ prevail, and because of clutter $P_F < P_{Fc}$. It has long been known for the problem we have set up here that[1]

$$P_F = \exp(-n\gamma/h\nu_0), \tag{46}$$

and

$$P_D = P_F^{1/(1+CNR)}, \tag{47}$$

where CNR is given by (23) with $2^{5/2}/\pi T f_{RES} = 1$. Thus, for example, $\geq$ 34 dB carrier-to-noise ratio suffices for $P_D = 0.99$ operation with $P_F = 10^{-12}$ in single-pixel target detection in the absence of clutter. When clutter is present and MTI is sought at velocities near zero km/h it is P_{Fc} not P_F that controls the system's false alarm rate.

To evaluate P_{Fc} we note that the assumptions we have made imply that

$$\Pr[R(f_D) \geq \gamma | \underline{r}(t) = \text{clutter} + \text{noise}, f_c = \delta]$$

$$= P_F^{1/[1 + CLNR(f_D - \delta)]} \tag{48}$$

where

$$\mathrm{CLNR}(f) = \frac{nE_c/h\nu_o}{[1+(\pi\sigma_c T)^2/2]^{1/2}} \exp\left[-\frac{(\pi f T/2)^2}{1+(\pi\sigma_c T)^2/2}\right], \qquad (49)$$

is the clutter-to-noise ratio at frequency detuning f. Averaging (48) over the f_c statistics yields the final result

$$P_{Fc} = \int_{-\infty}^{\infty} d\delta\, (2\pi\sigma_{fc}^2)^{-1/2} \exp[-(\delta-m_{fc})^2/2\sigma_{fc}^2]$$

$$\cdot P_F^{\,1/[1+\mathrm{CLNR}(f_D-\delta)]}. \qquad (50)$$

We have plotted P_{Fc} vs. CLNR, the clutter-to-noise ratio at zero detuning, in Fig. 8 for $P_F = 10^{-12}$, T = 20 μsec, σ_c = 30 kHz, m_{fc} = 0 Hz, σ_{fc} = 15 kHz, and two values of f_D (corresponding to $v_z = v_{RES}/2$ and $v_z = 1.5\, v_{RES}$, where $v_{RES} = 2^{3/2}\lambda/\pi T$ is the dwell-time limited velocity resolution). Fig. 8 shows the importance of clutter when trying for high-performance MTI at velocities comparable to the rms clutter velocity $\lambda(\sigma_c^2 + \sigma_{fc}^2)^{1/2}/2$.

4.0 EXPERIMENTAL RESULTS

In order to test various aspects of the models presented in Section 2.0, we have been examining the statistics[12] of target return and clutter data obtained with the MIT Lincoln Laboratory Doppler radar test bed[9]. We shall report herein some of our preliminary results.

---

12. Mesite, P. L., "Laser Speckle and Clutter Effects on Moving Targets Observed with an Optical Radar," S. M. Thesis, Dept. of Elect. Eng. and Comput. Sci., M.I.T., September 1983.

4.1 TARGET SPECKLE

A key feature of the target-return model described in Section 2.1 is the presumption that the envelope detected return from a moving rough-surfaced hard target should show laser speckle fluctuations. We tested this presumption by analyzing returns obtained with the Doppler test bed, from a truck-borne flame-sprayed aluminum calibration plate moving at constant velocity. Previous work[3,11] with the M.I.T. Lincoln Laboratory pulsed-imager test bed[13] had confirmed the diffuse nature of this calibration plate for stationary operation. Figure 9 shows a bar chart comprising an experimental histogram p(Y) of 450 spatially sampled normalized speckle plate returns Y taken by the Doppler radar with the target at 2.7 km range moving at about 24 km/h. Because the radar uses a linear envelope detector, these returns should be Rayleigh distributed (with the probability density shown by the curve in Fig. 9) if our assumed speckle model is correct[3]. A χ^2 goodness-of-fit test for the Rayleigh distribution on this histogram gives $\chi^2 = 9.426$ with 11 degrees of freedom, corresponding to a level of significance between 0.5 and 0.75 and excellent agreement between theory and data.

The Fig. 9 data were obtained in the far field of the Doppler radar. Similar measurements made at 0.27 km, which is the near field of the 13 cm diameter radar telescope, yielded histograms far too narrow to fit a Rayleigh distribution. This discrepancy was not due to saturation of the radar's electronics, nor could it be explained by scanning-induced decorrelation[12]; it is a subject of continuing research.

4.2 CLUTTER SPECTRA

The essential feature of the clutter model given in Section 2.2 is its distinction between micro-motion and macro-motion contributions to the frequency spectrum of clutter returns. To test this decomposition, we analyzed[12] clutter spectra obtained with the Doppler test bed from trees. Figure 10 shows an average of 7920 Doppler spectra from tree clutter at 0.5 km range obtained under 10-16 km/h wind conditions. As shown in this figure, the central peak is well fit by the Gaussian profile (15) with $m_{fc} = 0$ kHz and $\sigma = 43.3$ kHz; the region outside of the central peak is ascribed to a combination of SAW sidelobes and receiver noise.

13. Harney, R. C., and Hull, R. J., "Compact Infrared Radar Technology," Proc. SPIE 227, 162-170 (1980).

Figure 10 represents the composite of micro-motion and macro-motion effects. To separate these components in the data, each individual Doppler spectrum was windowed, to eliminate outlying points due to sidelobes and noise, and its average frequency shift computed. The windowed spectra were then shifted in frequency, so that their average frequency shifts all fell at zero, and averaged. The result of this procedure, shown in Fig. 11, represents the micro-motion of the clutter. As can be seen from this figure, the central peak is well fit by the Gaussian spectrum (13) with $\sigma_c = 33.1$ kHz. Finally, Fig. 12 shows the histogram of average frequency shifts for the 7920 windowed Doppler spectra. This histogram represents the macro-motion of the clutter, and is compared in Fig. 12 with the Gaussian density (see Section 2.2).

$$p_{fc}(\delta) = (2\pi\sigma_{fc}^{2})^{-1/2} \exp\left[-(\delta - m_{fc})^{2}/2\sigma_{fc}^{2}\right] \tag{51}$$

for the macro-motion instantaneous frequency shift. We see from Fig. 12 that (51) with $m_{fc} = 34.9$ kHz and $\sigma_{fc} = 35.6$ kHz gives a good fit to the data.

Figures 11 and 12 are not fully consistent with Fig. 10, i.e., the peak in Fig. 10 should be fit by a Gaussian centered at $m_{fc} = 34.9$ kHz with rms bandwidth $(\sigma_c^{2} + \sigma_{fc}^{2})^{1/2} = 48.6$ kHz according to Figs. 11 and 12 and the model of Section 2.2. Although the above rms bandwidth is not too far from the $\sigma = 43.3$ kHz value used in Fig. 10, the above center frequency cannot be correct as it corresponds to 27 m of net tree motion away from the radar over the 2.5 minute data acquisition period. Given the 33.7 kHz spacing between adjacent frequency samples in our Doppler spectra, plus the problems with sidelobes, noise, and speckle fluctuations, however, the m_{fc} discrepancy is not so unusual.

In addition to examining the spectral features of the tree clutter data, we have also considered[12] the amplitude fluctuations of the micro-motion contribution, which should be Rayleigh distributed according to the model in Section 2.2. Preliminary data analysis seems to indicate amplitude fluctuations may be better described by a lognormal rather than a Rayleigh distribution.

5.0 CONCLUSIONS

Laser radar signal models were presented for Doppler imagers and chirped-pulse range imagers. These models were used to assess the impacts of target decorrelation and laser frequency instability on the velocity and range resolution of long dwell time systems. The results indicated that decorrelation is a more severe problem than frequency instability. A clutter model, containing micro-motion and macro-motion components, was used to analyze the clutter-limited false alarm probability in single-pixel detection. The appropriateness of the preceding models was tested using data from the M.I.T. Lincoln Laboratory Doppler radar test bed. Reasonable confirmation was found for hard-target speckle in far-field operation, and the micro-motion/macro-motion decomposition of tree-clutter spectra.

ACKNOWLEDGMENTS

The laser radar data whose analysis was reported in Section 4.0 was supplied by D. G. Biron.

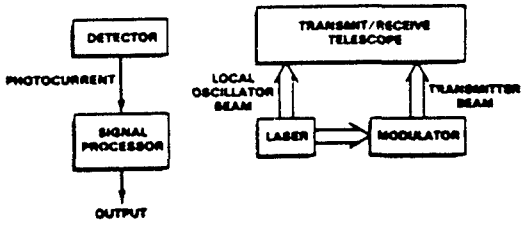

FIGURE 1. SYSTEM STRUCTURE FOR MONOSTATIC DOPPLER OR CHIRPED LASER RADAR.

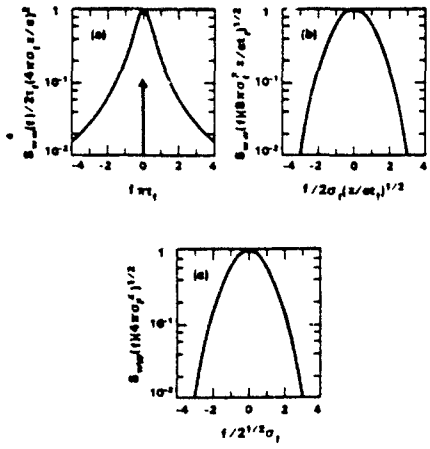

FIGURE 2. NORMALIZED SPECTRAL DENSITIES FOR THE LASER FREQUENCY-INSTABILITY EFFECT ON THE TARGET RETURN: (a) the very short range regime $2\sigma_f z/c << 1$, given by Eq. (11a); (b) the normal operating regime $2z/ct_f << 1$, $2\sigma_f z/c >> 1$, given by Eq. (11b); (c) the very long range regime $2z/ct_f >> 1$, given by Eq. (11c).

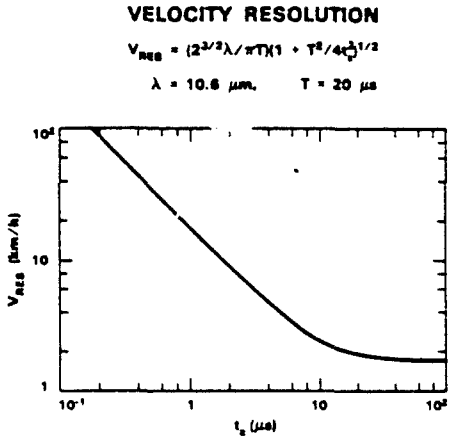

FIGURE 3. VELOCITY RESOLUTION V_{RES} vs. TARGET CORRELATION TIME t_c FOR A 10.6 μm WAVELENGTH 20 μsec DWELL TIME DOPPLER RADAR WITH NO FREQUENCY INSTABILITY.

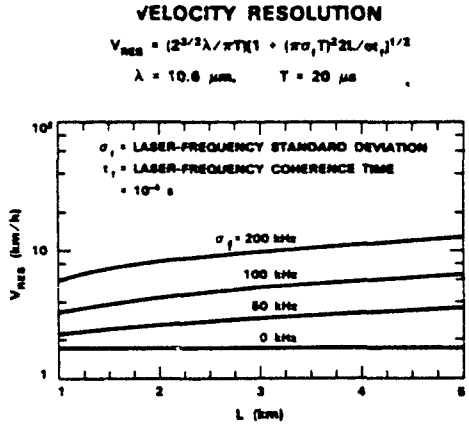

FIGURE 4. VELOCITY RESOLUTION V_{RES} vs. RANGE L FOR A 10.6 μm WAVELENGTH, 20 μsec DWELL TIME DOPPLER RADAR VIEWING A NON-DECORRELATING TARGET.

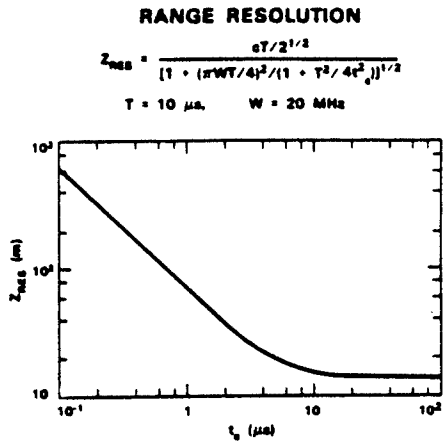

FIGURE 5. RANGE RESOLUTION Z_{RES} vs. TARGET CORRELATION TIME t_c FOR A CHIRPED LASER RADAR WITH 10 μsec CHIRP DURATION, 20 MHz CHIRP BANDWIDTH, AND NO FREQUENCY INSTABILITY.

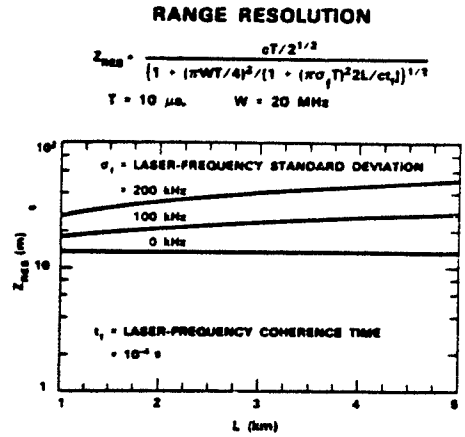

FIGURE 6. RANGE RESOLUTION Z_{RES} vs. RANGE L FOR A CHIRPED LASER RADAR WITH 10 μsec CHIRP DURATION AND 20 MHz CHIRP BANDWIDTH VIEWING A NON-DECORRELATING TARGET.

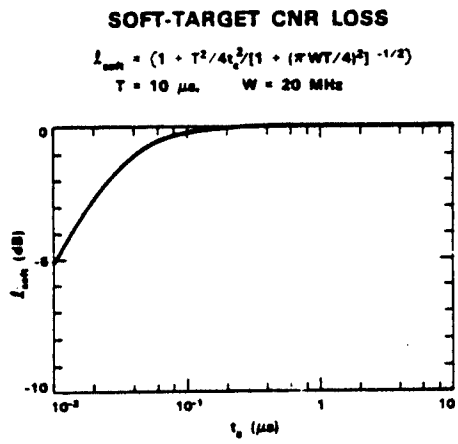

FIGURE 7. SOFT TARGET CNR LOSS ℓ_{soft} vs. TARGET CORRELATION TIME t_c FOR A CHIRPED LASER RADAR WITH 10 μsec CHIRP DURATION, 20 MHz CHIRP BANDWIDTH, AND NO FREQUENCY INSTABILITY.

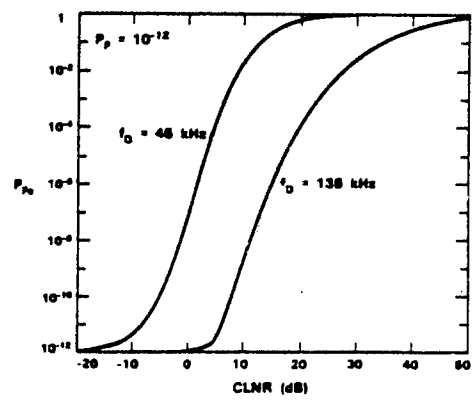

FIGURE 8. CLUTTER-LIMITED FALSE ALARM PROBABILITY P_{Fc} vs. CLUTTER-TO-NOISE RATIO AT ZERO DETUNING CLNR FOR TWO DOPPLER SHIFT FREQUENCIES f_D; $P_F = 10^{-12}$, T = 20 μsec, σ_c = 30 kHz, m_{fc} = 0 kHz, and σ_{fc} = 15 kHz.

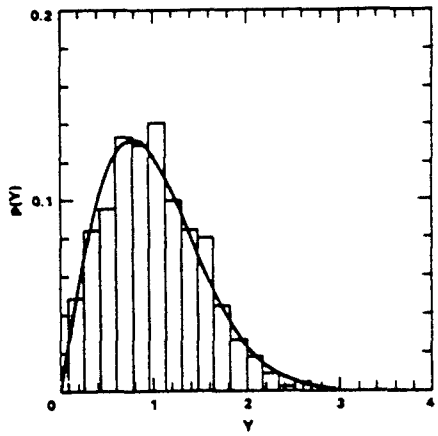

FIGURE 9. HISTOGRAM p(Y) OF TARGET RETURN AMPLITUDES Y FROM A MOVING SPECKLE TARGET (FLAME-SPRAYED ALUMINUM CALIBRATION PLATE); SMOOTH CURVE IS THE RAYLEIGH PROBABILITY DENSITY.

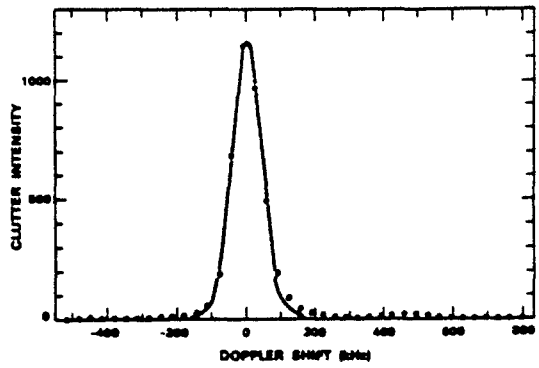

FIGURE 10. AVERAGE OF 7920 CLUTTER SPECTRA (POINTS) FROM TREES AT 0.5 km RANGE IN 10-16 km/h WIND CONDITIONS AND NORMALIZED GAUSSIAN (CURVE) FROM (15) WITH m_{f_C} = 0 kHz AND σ = 43.3 kHz FIT TO CENTRAL PEAK.

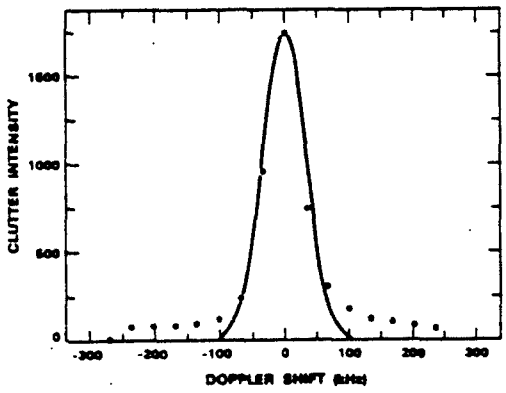

FIGURE 11. AVERAGE OF 7920 WINDOWED CLUTTER MICRO-MOTION SPECTRA (POINTS) FROM TREES AT 0.5 km RANGE IN 10-16 km/h WIND CONDITIONS, AND NORMALIZED GAUSSIAN (CURVE) FROM (13) WITH σ_C = 33.1 kHz FIT TO CENTRAL PEAK.

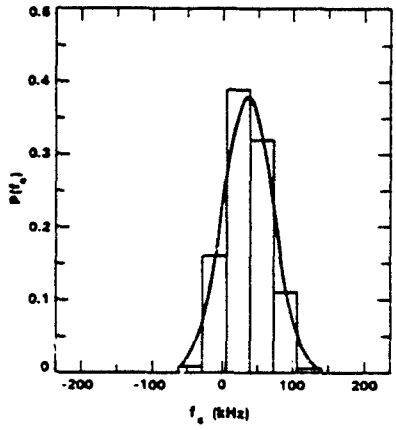

FIGURE 12. HISTOGRAM $p(f_C)$ OF MACRO-MOTION DOPPLER SHIFTS f_C OF 7920 CLUTTER SPECTRA FROM TREES AT 0.5 km RANGE IN 10-16 km/h WIND CONDITIONS: SMOOTH CURVE IS GAUSSIAN PROBABILITY DENSITY WITH m_{fC}= 34.9 kHz AND σ_{fC} = 35.6 kHz.

UNCLASSIFIED

SECURITY CLASSIFICATION OF THIS PAGE (When Data Entered)

REPORT DOCUMENTATION PAGE

READ INSTRUCTIONS BEFORE COMPLETING FORM

1. REPORT NUMBER
ESD-TR-83-238
ESL-TR-83-72

2. GOVT ACCESSION NO.
AD-A139448

3. RECIPIENT'S CATALOG NUMBER

4. TITLE (and Subtitle)
Coherent Laser Radar Remote Sensing

5. TYPE OF REPORT & PERIOD COVERED
Final Report
1 October 1982 — 30 September 1983

6. PERFORMING ORG. REPORT NUMBER

7. AUTHOR(s)
Robert J. Hull
David G. Biron
Stephen Marcus
Jeffrey H. Shapiro

8. CONTRACT OR GRANT NUMBER(s)
F1962.-80-C-0002

9. PERFORMING ORGANIZATION NAME AND ADDRESS
Lincoln Laboratory, M.I.T.
P.O. Box 73
Lexington, MA 02173-0073

10. PROGRAM ELEMENT, PROJECT, TASK AREA & WORK UNIT NUMBERS
Program Element No. 62601F
Project No. 1900

11. CONTROLLING OFFICE NAME AND ADDRESS
Air Force Engineering and Services Center,
Tyndall AFB, FL 32403

12. REPORT DATE
30 September 1983

13. NUMBER OF PAGES
68

14. MONITORING AGENCY NAME & ADDRESS (if different from Controlling Office)
Electronic Systems Division
Hanscom AFB, MA 01731

15. SECURITY CLASS. (of this report)
Unclassified

15a. DECLASSIFICATION DOWNGRADING SCHEDULE

16. DISTRIBUTION STATEMENT (of this Report)
Approved for public release; distribution unlimited.

17. DISTRIBUTION STATEMENT (of the abstract entered in Block 20, if different from Report)

18. SUPPLEMENTARY NOTES
None

19. KEY WORDS (Continue on reverse side if necessary and identify by block number)
laser waveform
coherent detection
aerosol backscatter
laser remote sensing
CO_2 laser

20. ABSTRACT (Continue on reverse side if necessary and identify by block number)

[U] This report summarizes the technical effort accomplished in FY83 on a program to make range-resolved measurements of chemical agents or pollutants distributed within the atmosphere. A description of the modified receiver electronics which permits rapid accumulation of a very large number of signal returns is described. The performance of a rapidly tunable CO_2 laser is discussed. Theoretical analyses of coherent laser radar systems including mixing efficiencies, speckle effects, and waveform performance are reported.

DD FORM 1473 1 Jan 73 EDITION OF 1 NOV 65 IS OBSOLETE

UNCLASSIFIED

SECURITY CLASSIFICATION OF THIS PAGE (When Data Entered)